Title: Inhibition of NFAT promotes loss of tissue resident uterine natural killer cells and attendant pregnancy complications in humans

Authors: Rebecca Asiimwe[1], Brittney Knott[1], Morgan E. Greene[1], Emma Wright[1], Markayla Bell[1], Daniel Epstein[1], Stefani D. Yates[1], Matthew D. Cheung[1], Michael V. Gonzalez[2], Samantha Fry[1], Emily Boydston[1], Stephanie Clevenger[3], Jayme E. Locke[1], James F. George[1], Richard Burney[3], Nitin Arora[4], Virginia E. Duncan[5], Holly E. Richter[3], Deidre Gunn[3], Aharon G. Freud[6], Shawn C. Little[1], Paige M. Porrett*[1]

Affiliations:

[1]Department of Surgery, Marnix E. Heersink School of Medicine, University of Alabama at Birmingham, Birmingham, AL, 35233 USA

[2]Center for Cytokine Storm Treatment & Laboratory, Department of Medicine, University of Pennsylvania, Philadelphia, PA, 19104 USA.

[3]Department of Obstetrics & Gynecology, Marnix E. Heersink School of Medicine, University of Alabama at Birmingham, Birmingham, AL, 35233 USA

[4]Department of Pediatrics, Marnix E. Heersink School of Medicine, University of Alabama at Birmingham, Birmingham, AL, 35233 USA

[5]Department of Pathology, Marnix E. Heersink School of Medicine, University of Alabama at Birmingham, Birmingham, AL, 35233 USA

[6]Department of Pathology, The Ohio State University, Columbus, OH 43210, USA

*Corresponding author: Paige M. Porrett (pmporrett@uabmc.edu)

Abstract: Uterine natural killer cells (uNKs) are a tissue resident lymphocyte population that are critical for pregnancy success. Although mouse models have demonstrated that NK deficiency results in abnormal placentation and poor pregnancy outcomes, the generalizability of this knowledge to humans remains unclear. Here we identify uterus transplant (UTx) recipients as a human population with reduced endometrial NK cells and altered pregnancy phenotypes. We further show that the NK reduction in UTx is due to impaired transcriptional programming of NK tissue residency due to blockade of the transcription factor nuclear factor of activated T cells (NFAT). NFAT-dependent genes played a role in multiple molecular circuits governing tissue residency in uNKs, including early residency programs involving AP-1 transcription factors as well as TGFβ-mediated upregulation of surface integrins. Collectively, our data identify a previously undescribed role for NFAT in uterine NK tissue residency and provide novel mechanistic insights into the biologic basis of pregnancy complications due to alteration of tissue resident NK subsets in humans.

One Sentence Summary: Role of NFAT in uterine NK cell tissue residency

Main Text:

INTRODUCTION

Successful pregnancy requires the interaction of multiple maternal immune cell types with uterine parenchymal cells and fetal placental trophoblast at the maternal-fetal interface (*1, 2*). Among the different immune cells that contribute to maternal and fetal health, uterine natural killer cells (uNKs) play key roles in multiple physiologic aspects of pregnancy, including (1) production of molecules to support fetal growth and development (*3, 4*); (2) trophoblast differentiation and placentation (*5*); and (3) uterine spiral artery remodeling (*6-22*), a process which transforms the uterine vasculature into a low pressure, high capacitance system thereby augmenting maternal blood flow to the placenta (*6, 23*). Importantly, mouse models have established that disruptions of uNK cell number or function result in pregnancy complications or loss, often due to abnormal placentation associated with poor spiral artery remodeling (*12, 13, 16, 24*). In humans, incomplete spiral artery remodeling in decidual biopsies has been similarly associated with structural placental abnormalities as well as clinical syndromes such as pre-eclampsia (*25, 26*). However, while a limited number of human studies have suggested that recurrent pregnancy loss is associated with an abnormal distribution of decidual NK cell subsets (*27*), pregnancy outcomes have not been well studied in individuals with known defects in NK cell number or function. Hence, the specific contribution of uNK cells to pregnancy complications in humans remains unclear.

A related knowledge gap that impairs our ability to understand pregnancy complications is the mechanism by which uNKs acquire tissue residence. Although a local, tissue-based precursor pool of hematopoietic cells may give rise to uNKs, a prior study which analyzed samples from uterus transplant recipients suggested that uNKs have a peripheral origin (*28*). These findings thus predict that uNKs acquire properties of tissue residency, such as expression of integrins which promote tissue retention, upon localization into the uterus. While other work has identified mechanisms of tissue residency in other human organs (*29-33*), mechanisms governing NK residence in the uterus are largely unexplored.

Organ transplant recipients represent an immunomodulated population who have reduced numbers of circulating NK cells (*34, 35*) and rates of pre-eclampsia that are six-fold greater than the general population (*36-41*). Despite the prevalence of pregnancy complications in organ transplant recipients, the biologic basis for this increased risk is unknown (*42*). Studies of uNKs in this at-risk population are notably absent, likely because of challenges associated with acquisition of samples and the frequency with which pregnancy is discouraged in this population (*43, 44*). Nevertheless, many of these barriers may be overcome in the setting of uterus transplantation, where transplantation occurs for the sole purpose of achieving pregnancy and live birth in patients suffering from absolute uterine factor infertility (*45, 46*). Notably, pregnancy complications such as pre-eclampsia are common in uterus transplant recipients (UTx) (*45-47*), suggesting that these individuals represent an opportunity to better understand the immune pathogenesis of pregnancy complications.

In this study, complementary single cell and imaging approaches were used to study uNKs derived from endometrial biopsies of healthy control volunteers (HC) and UTx. We found that UTx recipients possessed a reduced frequency of tissue resident natural killer cells (trNKs) that associated with clinical pregnancy complications and histologic placental abnormalities. Transcriptional programs of tissue residency in UTx trNKs were disrupted compared to HC trNKs, with impairment of TGFβ-mediated integrin expression as well as AP-1-based early tissue residency programs that are shared with murine CD8 T resident memory cells. Through comparative analyses of ex vivo samples as well as direct pharmacologic inhibition in vitro, we identified a previously undescribed role for NFAT in tissue residency programming of human uNK cells. Taken together, these studies link impaired tissue residency programming with defects in uNK abundance to improve our understanding of the pathogenesis of pregnancy complications in humans.

RESULTS

Reduced frequency of NK cells among endometrial immune cells in UTx

To begin our study of uNKs in human uterus transplant recipients, we performed serial secretory phase endometrial biopsies on two UTx >3 months after transplantation who had resumed normal menstrual cycling (5 biopsies) (table S1). UTx received standard pharmacologic immunosuppression as previously described (*45-47*); this included perioperative T-cell depletion with anti-thymocyte globulin as well as maintenance immunosuppression with a calcineurin inhibitor (i.e., FK506 / tacrolimus), an anti-proliferative agent (i.e., azathioprine), and an oral steroid (i.e., prednisone). Secretory

phase endometrial biopsies were collected from six HC volunteers (table S1) as this time point is when NK cells are most abundant (*48, 49*). Given the variable expression of CD56 across NK cell subsets, we assured capture of all NK cells by sorting CD45+ cells from endometrial biopsies and performing scRNA-seq (Fig. 1A). After data processing and Harmony integration (*50*), we analyzed 77,481 CD45+ endometrial immune cells from 11 biopsies, which included various lymphoid and myeloid populations such as NK cells, T cells, group 3 innate lymphocyte cells (ILC3s), B cells, mast cells, plasmacytoid dendritic cells, and monocytes/macrophages (Fig. 1A and fig. S1A).

We initially identified NK cell clusters among CD45+ endometrial immune cells by expression of conventional marker genes such as *NCAM1* (CD56) and *FCGR3A* (CD16) (Fig. 1B and fig. S1B). Clusters 0, 7, 8 and 21 comprised tissue resident NK (trNK) cells based on high expression of *ITGA1* and *NCAM1* (Fig. 1B), low expression of *FCGR3A* (Fig.1B), and expression of gene signatures associated with decidual NK cell subsets (i.e., dNK1, dNK2, dNK3) (*45*) (Fig. 1C). Meanwhile, conventional NK cells (cNK) with intermediate expression of *NCAM1* and high expression of *FCGR3A* were identified in cluster 3 (Fig. 1B), which also contained CD8 effector T cells sharing cytotoxic gene expression (Fig. 1B and fig. S1, C to E). In line with prior work (*46*), NK cells in uterus transplants were >90% recipient-derived (Fig. 1D), confirming that endometrial NK cells arise from blood-borne precursors. Expectedly, other immune cell subsets (i.e., T cells and myeloid cells) were also recipient-derived, while contaminating stromal and epithelial cells were >70% donor-derived (Fig. 1D). Although NK cells were abundant in HC endometrial biopsies, NK cells were significantly reduced among sequenced immune

cells in UTx biopsies compared to HCs (Fig. 1E). To validate these results, we used flow cytometry to further compare the frequency of uNK cells between UTx and HCs. Although tissue for flow cytometric analysis was available from only three of the five UTx biopsies, these analyses confirmed the statistically significant reduction in NK cell frequency among endometrial immune cells in UTx versus HCs (Fig. 1F).

Reduced NK cell density in UTx endometrium

The reduction in NK cell frequency among CD45+ endometrial immune cells in UTx could result from either a reduction in NK cell density in the tissue or from the presence of excess CD45+ non-NK cells. To determine whether NK cell density was reduced in UTx endometrium, we performed immunofluorescence microscopy to evaluate multiple fields of sections of endometrium from UTx and HCs. Biopsy sections (Fig. 2A) were stained with DAPI and anti-CD56 and data collected by epifluorescence (Fig. 2, B to F) at high resolution. Nuclei were segmented by custom semi-automated processing of the DAPI channel (see Methods) and assigned a status of positive or negative for CD56 expression (Fig. 2C and D). Multiple independent image fields were collected, each representing an area of about 0.13 mm^2 and containing 870±128 (mean ± SD) cells per field. The fraction of CD56+ cells was then calculated for each field (Fig. 2G to I).

CD56+ cells were observed either as isolated individuals or in groups (Fig. 2D). Counts of cells per field varied widely within the same biopsy (Fig. 2G), suggesting non-homogenous distribution of spatial cues directing NK localization in the tissue in both HC and UTx endometrium. By comparing the median values of the fraction CD56+ cells, we

found that NK cell density was reduced by roughly a factor of three in UTx biopsies (2.6% in HC versus 0.9% in UTx). P-values resulting from pairwise Mann-Whitney U tests showed that UTx samples tended to differ more from control than from each other (Fig. 2I). In contrast, the same analysis using anti-CD3 staining reveals that the density of CD3+ cells is reduced by about 40% in UTx compared to control (11% in control versus 7% in UTx; fig. S2). We conclude that NK cell density is reduced in UTx, supporting the observations from flow cytometry and scRNA-seq analyses.

Maternal vascular malperfusion in UTx placentae

We next considered the potential physiologic consequences of the reduction of NK cells on UTx recipients. We speculated that placentation would be altered in UTx given that spiral artery remodeling is impaired in mice with dysfunctional or deficient NK cells (*12, 13, 16, 24*), and inadequate spiral artery remodeling is associated with maternal vascular malperfusion (MVM) in humans (*8, 23, 26*). To test the hypothesis that placentation would be abnormal in UTx recipients, we examined placental histology in UTx recipients after delivery. Both placentas were small for gestational age at 236g (UTxA; 311-464g expected) and 223g (UTxB; 331-491g expected). H&E examination revealed patchy regions of increased syncytial knots and slender, sparse villi with widening of the intervillous space consistent with distal villous hypoplasia and accelerated villous maturation (Fig. 3A), a histologic phenotype indicative of MVM (*25, 51-53*). Notably, these histologic findings were identified in both UTx placentae but not HC (Fig. 3B). These histologic changes were associated with abnormal clinical courses in both UTx recipients. Both UTx recipients were delivered at ~34 weeks gestation due to pregnancy

complications: UTx “A” developed preterm premature rupture of membranes without evidence of acute chorioamnionitis, and UTx “B” developed pre-eclampsia with elevated blood pressure and serum creatinine. Notably, both clinical phenotypes have been associated with MVM (*51, 52*). Although more data are needed given the small number of UTx recipients in this study, these data align with reproductive phenotypes in NK deficient mice and suggest potential physiologic consequences for humans with reduced NK cell number.

Reduction of tissue resident NK subsets in uterus transplant endometrium

To investigate the mechanism of NK loss in UTx recipients, we first determined whether the NK cell reduction in UTx affected all uterine NK subsets equally. Consistent with prior studies (*54-56*), we identified two major populations of endometrial NK cells which could be distinguished by differential expression of *NCAM1* and *FCGR3A* (Fig. 1A and 4A) as well as transcriptional programs governing tissue residency and cytotoxic effector function (Fig. 4B and fig. S3). Tissue resident NK cells (trNK) expressed integrins and transcription factors frequently associated with tissue resident lymphocytes (i.e. *ITGA1, ITGAE, KLF6*) (Fig. 4B and fig. S3), whereas cNK expressed a variety of molecules associated with circulating populations, including *S1PR5* and *KLF2* (Fig. 4B and fig. S3) (*30-33, 57, 58*). Moreover, the endometrial tissue resident cluster expressed a gene signature associated with tissue residency in human lung NK cells (Fig. 4C and table S2 (*31*). Whereas cNK number and frequency were similar in UTx vs. HCs, trNK number and frequency were significantly reduced in UTx (Fig. 4, D and E). Because uterine trNKs are transcriptionally and functionally heterogeneous (*56, 59, 60*), we next determined if all trNK subsets were

reduced in UTx or whether the trNK defect was limited to specific trNK subsets. After identification of canonical trNK subsets by expression of decidual NK signatures (Fig. 1B) (*60*) and marker genes (Fig. 4F and table S2), we compared the frequency of individual trNK subsets between UTx and HCs. While HC and UTx had similar frequencies of trNK1 cells, we found statistically significant reductions in trNK2 and trNK3 frequency in UTx recipients (Fig. 4G). As tissue resident lymphocytes express adhesion molecules that promote tissue retention, we considered the possibility that tissue resident subsets may not be retrieved equally from endometrial tissue from HC vs. UTx. Because uterine trNK subsets in human decidua have been previously defined transcriptionally (*60*), we validated our scRNA-seq data by performing spatial transcriptomics on one healthy control biopsy and one uterus transplant biopsy. After deconvolution of the spatial transcriptomics data using cell2location (*61*) (fig. S4), we found reductions in all trNK subsets with relative preservation of cNK abundance in the UTx vs. HC (Fig. 4H). Taken altogether, these data suggest that the NK reduction in UTx endometrium is driven primarily by a loss of tissue resident NK cells.

Altered transcriptional programming of canonical tissue residency in trNK from UTx

Having established that trNK cells were reduced in UTx compared to HCs, we aimed to understand the molecular mechanisms responsible for this reduction. To test the hypothesis that transcriptional programs of trNK development were altered in UTx trNK, we performed CITE-seq analysis on CD45+ cells aggregated from three HC and four UTx endometrial biopsies (table S1). As CITE-seq analysis of uNKs has not yet been reported,

we first characterized uNK subsets with this methodology. NK cells were identified among CD45+ endometrial immune cells based on their gene expression as well as protein surface phenotype (i.e., CD56+CD14-CD3-) and were re-clustered for downstream analyses. As in our prior analyses, NK cells resolved into two major groups of cNK and trNK subsets which were largely distinguished by differential expression of genes associated with cytotoxicity (fig. S5A) as well as reciprocal expression of CD49a (*ITGA1*) and CD16 (*FCGR3A*) (Fig. 5, A and B, and fig. S5, A and B). cNK and trNK subsets were further distinguished by variable expression of CD56, CD45RA, and KLRG1 among other genes and proteins (fig. S5, A to C). While CD49a- NK cells were composed mostly of $CD56^{dim}$CD16+ cNKs (fig. S5B), CD49a+ cells contained multiple distinct subsets, including trNK1, trNK2, and trNK3 as well as proliferating cells (Fig. 5C and fig. S5, D and E). Our analysis leveraging both cell surface protein expression and single-cell transcriptomics further distinguished multiple trNK2 and trNK3 subsets which shared core trNK signatures (fig. S5F) yet varied from one another based on expression of effector molecules (i.e., *GNLY, GZMA*), chemokine ligands (i.e., *CCL3, CCL4, CCL5*) and integrins (*ITGAX, ITGAD*) (fig. S5D).

Next, we compared endometrial trNK subsets among HC and UTx samples. As in our prior analyses, we noted that tissue resident subsets were less frequent among UTx CD56+ NK cells compared to healthy controls (Fig. 5D). Moreover, CD103+ trNK3 subsets (C0&C5) were preferentially and markedly reduced in UTx (Fig. 5D), resulting in an overall skewing of the trNK compartment toward trNK1 cells (Fig. 5D). Given the critical role of TGFβ in CD103+ tissue resident lymphocyte development (*30, 58, 62-64*), we

hypothesized that TGFβ target genes were downregulated in trNK3 cells from UTx vs. HCs. Indeed, the TGFβ gene signature was downregulated in UTx trNK3 subsets (Fig. 5E), including the integrins *ITGA1* and *ITGAE*, as well as *CD9* and *ITGB7* (Fig. 5F). Accordingly, the surface expression of the corresponding proteins was also reduced in UTx trNK3 subsets (Fig. 5G), suggesting that cells which possessed trNK3 transcriptomes in UTx had an overall shift in their surface proteome toward trNK2 subsets (Fig. 5H). Collectively, these data suggested that disruption of TGFβ-mediated tissue residency programming in UTx samples resulted in an overall reduction of trNK3 subsets with transcriptional skewing toward trNK1 cells. Notably, changes in cellular transcriptomes corresponded to changes in surface phenotype, which was independently confirmed by flow cytometry (Fig. 5I).

Reduced expression of early trNK developmental program in UTx

Although the contribution of TGFβ to tissue residency programming is well established (*30, 58, 62-64*), less is known about the temporal orchestration of transcriptional programs of residency as lymphoid cells seed tissues from the blood. Importantly, recent work in a mouse model of LCMV infection has suggested that an array of immediate early response genes (i.e., *JUN*, etc.) are not only expressed early after tissue entry but are required for tissue residence (*65*). Moreover, prior work investigating human uterine NK development has suggested that a similar transcriptional program of early tissue adaptation is upregulated in early endometrial immigrants after arrival from the blood (*56*). We thus tested the hypothesis that trNKs were reduced in UTx due to defective

expression of this early developmental program (EDP) that is conserved between species and cell types (table S2).

First, we examined expression of the tissue resident EDP in healthy control trNK and cNK subsets and found highest expression of the EDP in certain trNK clusters (i.e., C5, C6, C7) (Fig. 6A). Although expression of the tissue resident EDP varied across trNK subsets in healthy controls (Fig. 6, A&B), we found a statistically significant reduction of expression of the EDP signature in virtually all UTx trNK clusters (Fig. 6B). Further examination of the most highly expressed EDP genes revealed two gene modules which were reciprocally expressed among trNK1 and trNK3 subsets (Fig. 6C). trNK2 subsets had intermediate expression of both gene modules, suggesting an intermediate transcriptional state between trNK1 and trNK3 cells, in line with prior results (*56*). Notably, trNK2 and trNK3 subsets were distinguished from trNK1s in part by increased expression of the developmental module composed of AP-1 transcription factors (i.e., developmental module 2) (Fig. 6D), a feature we dissected further after grouping similar trNK subsets (Fig. 6D, left). These analyses revealed that the developmental module encompassing AP-1 transcription factors (i.e. developmental module 2) was significantly less expressed in UTx trNKs than in HCs (Fig. 6D). In contrast, the developmental module which predominated in trNK1 cells (i.e., developmental module 1) had much more modest reductions in expression in UTx vs. HC (Fig. 6D). Collectively, these results demonstrate that the early core developmental programming of tissue residency is impaired in UTx endometrial NK cells, with larger reductions in trNK2 and trNK3 cells which had higher expression of AP-1 based developmental tissue residency programs.

Role for NFAT in tissue residency programming in uterine NK cells

We next considered the mechanism by which transcriptional programming of uterine natural killer cell tissue residency was disrupted in UTx. Because NFAT regulates CD103 gene expression (*66*) and NFAT-dependent genes have been identified within prior studies of tissue resident lymphocytes (*56, 67*), we hypothesized that tissue residency programming was reduced in UTx due to exposure of these individuals to immunosuppression drugs which prevent NFAT nuclear translocation (i.e., calcineurin inhibitors; tacrolimus). We tested for overlap of a curated gene set of NFAT targets (table S2) with genes upregulated during mucosal CD8 T_{RM} differentiation (*65*) and found 42 genes governing lymphocyte tissue residency that could be influenced by NFAT (Fig. 7A). Having identified NFAT-dependent genes involved in the transcriptional programming of tissue residency (i.e., $NFAT^{TR}$ signature), we then tested for enrichment of the $NFAT^{TR}$ signature in endometrial trNK from healthy control volunteers and found statistically significant enrichment of multiple $NFAT^{TR}$ genes in human endometrial trNK compared to cNK cells (Fig. 7, B and C). We next determined whether the $NFAT^{TR}$ signature was differentially expressed in endometrial NK cells from uterus transplant recipients versus healthy controls. We compared UTx with HC NK cells within each major trNK cluster and then tested for enrichment of the $NFAT^{TR}$ signature among the resulting differentially expressed genes. These analyses revealed enrichment of the $NFAT^{TR}$ signature among genes downregulated in UTx compared to HCs in trNK subsets reduced in UTx (i.e., trNK2 and trNK3 subsets) (Fig. 7D). We noted strong conservation of $NFAT^{TR}$ genes that were downregulated in affected UTx subsets (Fig. 7D). Notably, the $NFAT^{TR}$ genes

downregulated in affected UTx subsets corresponded to genes shared in the developmental program most expressed in trNK2 and trNK3 subsets (Fig. 7, E and F). Collectively, these data suggest a role for NFAT in tissue residency programming of endometrial trNK cells and identify reductions in trNK subsets with highest expression of transcriptional developmental programs that are enriched for NFAT-dependent genes.

IL-15 promotes integrin expression in endometrial trNK cells through NFAT

Although NFAT has well-established roles conveying signals downstream of antigen receptors in B and T lymphocytes (*68*), less is known about how innate cells such as NK cells use NFAT to translate environmental inputs. Nevertheless, a small number of prior studies have identified NFAT effects downstream of cytokine receptor signals such as IL-6 (*69*) and IL-15 signals (*70*). Since IL-15 synergizes with TGFβ in NK cells to promote upregulation of integrins important in tissue residency (*71*), we hypothesized that NFAT was contributing to tissue residency programming of trNK cells downstream of IL-15 signals. To test this hypothesis, we tested whether NFAT blockade by FK506 would result in impairment of key integrins on endometrial NK cells in response to IL-15 stimulation. IL-15 stimulation in vitro for 4-7 days was sufficient to induce significant upregulation of CD103 and CD49a expression on endometrial NK cells without the addition of exogenous TGFβ (Fig. 8A). However, the addition of FK506 to these cultures significantly diminished the frequency of CD103+CD49a+ endometrial trNK cells, with concomitant increases in the frequencies of CD103-CD49a+ and CD103-CD49a- cells (Fig. 8B). Altogether, these in vitro studies suggest that cytokine signals which mediate tissue residency programs in endometrial trNK utilize NFAT.

DISCUSSION

Significant knowledge gaps remain regarding our understanding of the immune pathogenesis of pregnancy complications in humans. Although mouse models have firmly established the role played by uNKs in spiral artery remodeling and placentation (*7, 12, 13, 16, 24*), pregnancy outcomes in women with reductions in endometrial NK cells have not been described. In this work, we identify uterus transplant recipients as an at-risk cohort who possess a reduced and skewed complement of tissue resident NK cells. Reductions in trNK number in longitudinal endometrial biopsies collected prior to pregnancy in UTx recipients were associated with pregnancy complications and histologic placental abnormalities characteristic of maternal vascular malperfusion. Analysis of trNK transcriptional and proteomic signatures in UTx samples not only revealed reduced expression of individual integrins critical for lymphocyte residency in mucosal tissues (*30-33, 57, 58, 62-65, 72*), but also revealed reductions in NFAT-dependent gene modules that govern early trNK development (*65*). Collectively, these data suggest that UTx recipients may recapitulate reproductive phenotypes observed in mice with inadequate NK cell number or function, thus deepening our understanding of the pathogenesis of pregnancy complications in humans.

Our work contributes new insights to the molecular events which guide the development of tissue resident natural killer cells. Although NFAT is known to bind the *ITGAE* enhancer (*66*) and contributes to CD103 expression in CD8 T cells after TCR stimulation (*73*), a role for NFAT in regulating CD103 expression in NK cells has not yet been described. We

hypothesized that in the absence of an antigen receptor, NFAT would promote CD103 expression in uterine NK cells downstream of a cytokine signal, as has been described previously for IL-6 (*69*) and IL-15 (*70*). In this work, we tested the hypothesis that IL-15 could promote CD103 expression through NFAT-dependent mechanisms given that IL-15 is secreted by decidualizing stromal cells in the secretory phase (*74, 75*). Moreover, IL-15 is known to synergize with TGFβ to induce CD103 expression on peripheral blood NK cells through MAPK pathways (*71*). Although NFAT is indeed a target of MAPK in T cells (*76*), it is unclear what intracellular molecules are promoting NFAT-dependent CD103 expression in endometrial trNK3 cells, as NFAT may be acting downstream of IL-15-mediated PI3K activation as well. Additional studies will be needed to elucidate the molecular details of NFAT signaling on CD103 expression by trNK3 cells, but this work will likely be highly impactful given the severity of the trNK3 defect we observed in UTx endometrium.

While the sensitivity of CD103-expressing trNK3 cells to NFAT inhibition may largely be explained by the role of NFAT in *ITGAE* gene expression, the reduced frequency of CD103- trNK2 cells in UTx endometrium required further explanation. As our understanding of tissue resident immune cells has expanded well beyond the adhesome in recent years, we considered the possibility that other molecular subroutines of tissue residency were impacted by NFAT. Unexpectedly, we found significant overlap between genes upregulated early in tissue residency with a curated list of NFAT targets, suggesting a potential mechanism for loss of CD103- subsets in UTx endometrium. Nevertheless, not all trNK subsets equally expressed the NFAT-dependent early tissue

residency program, thus providing an explanation for the relative sparing of the trNK1 subset while trNK2 and trNK3 cells were reduced. Precisely how NFAT promotes expression of the early residency signature in trNK2 and trNK3 cells remains to be investigated, and in pursuit of this question, the NFAT-independence of trNK1 subsets may also be deciphered. We anticipate that additional clues will become available as our understanding of the specific environmental signals which propel trNK1 differentiation is improved over time.

Reduction of trNK subsets in uterus transplant recipients in our study cohort was associated with placental pathology and clinical syndromes associated with aberrant spiral artery remodeling. Taken together, these findings suggest that there are potentially significant consequences to disruption of tissue residency programming of NK cells on pregnancy outcomes in humans. Nevertheless, robust conclusions based on these associations are limited by the small sample size of our UTx cohort and the absence of decidual studies to assess the magnitude of spiral artery transformation. Such structural studies on future UTx recipients will be necessary to fully interpret our findings and place this work in a larger context. Moreover, while we attributed the NK reduction observed in this work to aberrant residency programming in the setting of NFAT inhibition, UTx recipients are on a variety of immunosuppression agents whose effects on trNK recruitment, survival, differentiation, or function have yet to be tested. Additional studies will be needed to discriminate between these possibilities and determine how these factors play a role in endometrial immune homeostasis. Finally, our work does not preclude a role for uterine parenchymal dysfunction or altered decidualization in UTx

recipients due to FK506 effects. Thus, expansion of our study to diverse cell types in other organ transplant recipients will be necessary to complete our understanding of pre-eclampsia pathogenesis in this setting. Additional examination of the NFAT axis in trNKs in other at risk populations will be key to determine the potential benefit of therapeutic modulation of this pathway.

MATERIALS AND METHODS

Study Design

Research objective:

To test the hypothesis that uterine NK cells are abnormal in a recipient population at elevated risk for pregnancy complications.

Research location: All aspects of the study (i.e., subject recruitment, sample collection, and sample analysis) were performed at the University of Alabama at Birmingham (UAB).

Research subjects:

<u>Healthy control (HC) participants</u> were screened for inclusion and exclusion criteria ahead of their gynecology clinic visits at UAB. Once eligibility was confirmed, participants were approached for written informed consent for study participation. Inclusion criteria consisted of reproductive age, uncomplicated pregnancy history, normal menstrual cycles, and absence of serious medical illness. Exclusion criteria included any history of the following: current pregnancy, malignancy, diabetes, pharmacologic immune modulation, systemic autoimmune disease, prior organ or bone marrow transplant, history

of chemotherapy or radiation treatment, chronic or end-stage organ disease, history of HIV/HBV/HCV infection, instrumentation of the uterine cavity (i.e., D&C) within prior 12 months, use of an intrauterine device in prior 3 months, oral contraceptive use in prior 3 months, pregnancy within prior 12 months, NSAID or aspirin use within the prior 10 days, and/or medical contraindication to NSAIDs. CMV serostatus was not determined for healthy control participants. Healthy control participants underwent HCG testing in the clinical space prior to endometrial biopsy to document a negative pregnancy test.

Uterus transplantation is offered as standard of care treatment outside of a clinical trial at UAB for XX genotype individuals with absolute uterine factor infertility who meet selection criteria. Uterus transplant recipients were screened for participation in the endometrial immunobiology study during clinic visits at UAB. Once eligibility was confirmed, participants were approached for written informed consent for study participation. Endometrial biopsies were collected from participants >30 days post-transplant with normal menstrual cycles and no evidence of infection. Both participants were Caucasian individuals of reproductive age who met transplant center criteria; specific ages are not reported given the small nature of the patient cohort. Etiology of uterine factor infertility included hysterectomy as well as congenital absence of the uterus. PBMCs were collected one day prior to transplantation for whole exome sequencing. Both participating transplant recipients received a blood group compatible transplant from a deceased donor of reproductive age. Transplant recipients received induction immunosuppression with anti-thymocyte globulin (6mg/kg) and 500mg of intravenous methylprednisolone at the time of transplantation. Maintenance immunosuppression consisted of tacrolimus, azathioprine,

and prednisone. Target levels of tacrolimus were 5-10 ng/mL and were tested weekly. Secretory phase endometrial biopsies were obtained while protocol cervical biopsies were performed for immunologic monitoring of the graft. No endometrial biopsy was included in the study from a patient treated for rejection based on cervical biopsy findings. Additional medications taken during the first six months of transplantation included daily sulfamethoxazole/trimethoprim (for PCP prophylaxis) as well as acyclovir (UTxB) and valganciclovir (UTxA). Acyclovir was taken for HSV prophylaxis by UTxB given that both the recipient and the donor were seronegative for cytomegalovirus (CMV). UTxA was prescribed valganciclovir as she and her donor were both CMV seropositive. All endometrial biopsies from UTx recipients were obtained >30 days after transplantation after resumption of normal menstrual cycles but prior to embryo transfer (table S1). Placentas were examined immediately after cesarean delivery from both participants.

Slides from a healthy control archived placenta that was matched for gestational age (~34 weeks) with UTx deliveries were retrieved from an internal biorepository and evaluated by a perinatal pathologist (V.E.D.).

Brain-dead deceased donors provided 1) blood for whole exome sequencing, and 2) endometrium for in vitro co-culture experiments. Deceased donors were identified by Legacy of Hope personnel for the purpose of organ transplantation and/or research, and families of the deceased donors provided authorization. PBMCs were collected from deceased donors (n=2) prior to uterus procurement for the purposes of transplantation in order to perform donor genotyping through whole exome sequencing. Endometrium for in

vitro co-culture experiments was obtained from deceased donor hysterectomies (n=4) that were performed during surgical training procurements but were not transplanted. Data on the menstrual cycle phase for the four deceased donor endometrial samples was unavailable.

Experimental Design

Design Synopsis: Human endometrium was sampled from 1) healthy control participants (secretory phase), 2) uterus transplant recipients (secretory phase), and 3) brain-dead deceased donors (unknown menstrual cycle phase) for this study. Endometrial samples were analyzed with single cell approaches (i.e., scRNA-seq, CITE-seq, flow cytometry) as well as imaging (i.e., spatial transcriptomics, immunofluorescence microscopy). Single cell suspensions of endometrium were cultured with IL-15 and FK506 for 3-7 days.

Rigor & reproducibility considerations

Healthy control and uterus transplant participants used an ovulation predictor kit (Clearblue® digital ovulation tests (SPD Swiss Precision Diagnostics GmbH; Item number 245-03-0301)) to objectively identify the secretory phase of the menstrual cycle. Menstrual cycle dating was therefore not dependent on subject reporting based on the start date of menses. Of note, the digital ovulation predictor kit turns positive when luteinizing hormone (LH) is detected in the urine. Participants were brought into the clinic to undergo endometrial biopsy in the days following the LH surge, and biopsy data are thus reported as “LH+7” to denote menstrual cycle day after the LH surge. Variability in

the uterus transplant data were minimized by collecting biopsies >30 days after transplantation only from individuals who had resumed normal menstrual cycles.

Use of Biologic and Technical Replicates: For single-cell RNA-seq experiments, six secretory phase endometrial biopsies were obtained from six independent individuals (for healthy controls), and five secretory phase endometrial biopsies were obtained from two independent individuals who had received a uterus transplant (table S1). Endometrial biopsies were initially analyzed separately and then analyzed together after Harmony integration to control batch effects. For ex vivo flow cytometric analyses, three secretory phase endometrial biopsies were obtained from two independent individuals, and 16 secretory phase endometrial biopsies were obtained from healthy control volunteers. For in vitro co-culture experiments, four secretory phase endometrial biopsies were obtained from healthy control volunteers and four endometrial biopsies were obtained from deceased donor hysterectomies (unknown menstrual cycle date). In vitro co-culture experiments were performed in duplicate or triplicate. For spatial transcriptomics analyses, two sections were performed for each participant (one healthy control volunteer and one uterus transplant recipient). Results from one section per participant are reported in the manuscript but are representative of both sections. For immunofluorescence microscopy analyses, secretory phase biopsies were obtained from two individual healthy control volunteers, and three secretory phase biopsies were obtained from two individual uterus transplant recipients. Although sample number was limited in this study, the entirety of the tissue was assessed with multiple sections evaluated by an automated

approach with ~10% error. Data from all individual biologic replicates are provided in the visualizations.

Regulatory considerations:

The University of Alabama at Birmingham Institutional Review Board reviewed and approved sample collection from healthy control participants under project “Mechanisms of Uterine NK Cell Differentiation” (IRB-300006859) and sample collection from uterus transplant recipients under project “Endometrial Immunobiology in Uterus Transplantation” (IRB-3000007980). All samples were de-identified.

Sample collection & processing

Endometrial biopsies

Secretory phase endometrial biopsies were collected with a Pipelle® suction curette (Cooper Surgical; Ref. 8200) in the clinical setting and transported to the laboratory in DPBS with calcium and magnesium ($DPBS^{+/+}$; Gibco™; Cat. 14-040-133) on ice. Multiple passes of the suction curette were performed to acquire sufficient tissue for multimodal analysis with processing described below. Endometrial biopsies were then digested to isolate cells for downstream analysis including sorting, flow cytometry, or in vitro incubation.

<u>Endometrial biopsies used for imaging analyses</u>, including spatial transcriptomics and immunofluorescence microscopy, were frozen according to 10x Genomics CG000240 Demonstrated Protocol for Visium Spatial Tissue Preparation Guide. The biopsy pieces

were embedded in O.C.T. mounting media (Tissue-Tek; Cat. No. 4583) in a mold (Tissue-Tek; Cat. No. 4566). Molds were then placed in liquid nitrogen-cooled isopentane (Fisher Scientific; Cat. No. O3551-4). Frozen molds were stored at -80°C until sectioned onto Visium slides or glass slides for immunofluorescence microscopy.

Endometrial biopsies used for single cell isolation (i.e., scRNA-seq, flow cytometric analysis, in vitro co-culture) were minced with a razor blade on ice and transferred to a 50 mL conical tube on ice. The biopsy had 4 mL of 37°C-warmed digestion buffer added ($DPBS^{+/+}$ + 40 mL 5 mg/mL Liberase (Sigma Aldrich; SKU 5401127001) + 4 mL 1 mg/mL DNAse I (Sigma-Aldrich; SKU 11284932001)). Digestion was performed in a 37°C shaking incubator at 240 RPMs for 20 minutes. The digested sample was filtered through a 70 µm strainer (Stemcell Technologies; Cat. 27260). The strainer was rinsed 5 times with 1 mL ice-cold $DPBS^{+/+}$. The digested biopsy was then centrifuged at 300xg for 5 min at 4°C. The cell pellet was incubated in 3 mL ACK lysis buffer (Quality Biological; Cat. 118-156-101) on ice for 2 minutes. After ACK lysis, 12 mL ice-cold DPBS without calcium and magnesium ($DPBS^{-/-}$; Gibco™; Cat. 14-287-080) was added to the cell suspension. The cells were then centrifuged at 300xg for 5 min at 4°C. The buffer was removed and 0.5-1mL fresh sort buffe (ice-cold $DPBS^{-/-}$ + 0.04% (w/v) BSA (Jackson ImmunoResearch; Cat. 001-000-162)), was added. The cells were then suspended and counted. All cells were counted by the following method: 10 µL of cell suspension from samples was added to 90 µL 0.04% Trypan blue in PBS (Gibco™; Ref. 15250-061) for a 1:10 dilution, or serially diluted to make a 1:100 dilution. Cell counts were performed using a disposable

Neubauer improved hemocytometer (INCYTO; DHC-N01-5), following the manufacturer's instructions for loading.

Placental processing

Placentas were recovered from the operating room at time of delivery and placed in a sterile plastic container for transport to the clinical surgical pathology laboratory. Placentas were processed according to the Amsterdam Criteria (Amsterdam Placental Workshop Group Consensus professional guidelines) and evaluated by an experienced perinatal pathologist (V.E.D.). In brief, the placental disk was sequentially sectioned and systematic random samples of the chorionic plate, the mid-zone, and the basal plate were collected and placed in 10% formalin. Samples were subsequently paraffin embedded, stained with hematoxylin and eosin, and sectioned at 5µm for histopathologic analysis.

PBMC processing

PBMCs were isolated to perform whole exome sequencing (WES). Blood was collected in EDTA-K2 tubes vacutainers (BD and Company; Ref. 366643) and blood collection set (MYCO Medical Supplies, Inc.; Ref. GSBCS23G-7T). PBMC isolation was performed at room temperature until red blood cell (RBC) lysis. Equal volumes of wash media (DPBS$^{-/-}$ + 2% (v/v) FBS (Gemini Bio; Ref. 100106)), were added to the whole blood and mixed. The manufacturer's instructions were followed to isolate PBMCs using Lymproprep™ (Stemcell Technologies; Ref. 07811) and either a Sepmate™-15 or -50 (Stemcell; Ref. 85420 or 85450), depending on the blood volume. Once the PBMCs were isolated, the cells were washed with the DPBS$^{-/-}$ and 2% FBS two times, centrifuged once at 300xg for

8 minutes and once at 120xg for 10 minutes with no break. After removing the final wash buffer, RBCs were lysed using 3 mL of room temperature ACK lysis buffer (Quality Biological; Cat. 118-156-101) for 2 minutes on ice. Ice-cold DPBS was added to the 14 mL mark and mixed to finish the lysis reaction. Cells were pelleted by centrifugation, 400xg for 5 minutes at 4°C. The buffer was removed and 0.5-1mL DPBS$^{-/-}$ was added; the cells were suspended and counted. PBMCs were cryopreserved until thawed for DNA isolation and subsequent whole exome sequencing.

Deceased donor hysterectomies

Surgical hysterectomy for the purposes of research was performed in the Donor Recovery Center at the University of Alabama at Birmingham from deceased donors after family authorization for research was obtained. Deceased donor uteri were recovered after donor cross clamp and removal of other organs for the purposes of transplantation. Uteri were transported to the laboratory on ice and bivalved to expose the endometrium. A scalpel blade was used to gently scrape the endometrium into a culture dish, and the sample was washed and digested as above for flow cytometric and/or in vitro co-culture experiments.

Flow cytometric analysis & cell sorting

Live, CD45+ immune cells were used for scRNA sequencing and were prepared for FACS-sorting from endometrium as follows: Cells were first stained using the 150 µL 1:600 LIVE/DEAD™ Fixable Aqua stain kit (Molecular Probes™; Cat. L34957) diluted in DPBS$^{+/+}$ on ice for 30 minutes. After the incubation, cells were centrifuged at 300xg for 5

minutes at 4°C, and the buffer aspirated. Cells were then washed in staining buffer (DPBS$^{+/+}$ + 2% FBS + 0.4% (v/v) + 0.5 M EDTA (Fisher Scientific; Cat. No. AAJ15694AP)). Cells were pelleted and then resuspended in staining buffer and stained for 30 minutes on ice with 1 mg/mL AF700-mouse-anti-human CD45 (BioLegend; 368508) and PE-mouse anti-human CD235a in staining buffer. After antibody staining, cells were centrifuged at 300xg for 5 minutes at 4°C and the staining buffer aspirated. Cells were washed in 1 mL ice-cold sorting buffer and then centrifuged at 300xg for 5 minutes at 4°C. The wash buffer was then removed, and the cells were resuspended in ice-cold sorting buffer at a concentration of 2-7 million cells/mL. Live CD45+ CD235a- cells were then sorted on a FACSAria I or II (BD Biosciences) at the UAB Flow Cytometry Core Facility in tubes with 5 mL sorting buffer in the bottom. Cells were counted again to determine cell number, concentration, and viability.

Cells prepared for flow cytometric analysis were aliquoted to have between 200,000 – 10,000,000 cells per tube. Cells were stained first in 150 µL LIVE/DEAD™ Fixable Aqua using the staining kit described above. Cells were then resuspended in 50 mL staining buffer on ice, which included 30 mL of BD Brilliant Stain Buffer (BD Biosciences; Cat. No. 563794) and 1 mL 400 mg/mL Pacific Blue-mouse-anti-human CD45 (BioLegend; Cat. No. 304029; clone HI30), 1 mL 50 mg/mL PE/Dazzle594-mouse-anti-human CD16 (BioLegend; Cat. No. 302054; clone 3G8), 1 mL 100 mg/mL PE/Cy7-mouse-anti-human CD39 (BioLegend; Cat. No. 328212; clone A1), 1 mL 50 mg/mL APC-mouse-anti-human CD56 (BioLegend; Cat. No. 318310; clone HCD56), 0.5 mL 200 mg/mL APC/Cy7-mouse-anti-human CD3 (BioLegend; Cat. No. 317342; clone OKT3), 2 mL 200 mg/mL BV711-

mouse-anti-human CD49a (BD Biosciences; Cat. No. 742361; clone SR84), and 1 mL 70 mg/mL BV421-mouse-anti-human CD103 (Biolegend; Cat. No. 350214; clone Ber-ACT8). After the incubation, cells were centrifuged at 300xg for 5 minutes at 4°C and the buffer aspirated. Cells were then washed in 1mL ice-cold staining buffer. The cells were centrifuged at 300xg for 5 minutes at 4°C and the buffer aspirated. Cells were resuspended in DPBS for flow cytometric analysis on a Cytek Northern Lights spectral cytometer.

In vitro culture

Single-cell suspensions of endometrium were resuspended in complete media and plated in 24 well plates with 10 ng/mL IL-15 ± 10 ng/mL FK506. $5x10^5$ – $1x10^6$ cells were plated in duplicate or triplicate and cultured in a 5% CO_2 incubator for 3-7 days. Culture media was replaced with fresh IL-15 ± FK506 at day three for 7 day cultures. Upon culture completion, cells were recovered from the plate and subjected to flow cytometry analysis as described above.

Whole exome sequencing

PBMCs used for whole exome sequencing (WES) were collected from uterus donors and recipients prior to uterus transplantation. PBMCs were cryopreserved, as described above, and then thawed for WES. Cryopreserved cells were partially thawed in a 37°C water bath while gently swirling. When half of the volume of the cells were thawed, 500 mL of 37°C-warmed thawing media, RPMI with 10% FBS, was added to the cryovials. Suspended cells were transferred to a 15 mL conical tube with 9 mL of warmed thawing

media. Cells were centrifuged at 400xg for 5 minutes at 4°C. The thaw media was aspirated, and cells were washed again in thaw media. After centrifugation as before, thaw media was aspirated, and cells were suspended in $DPBS^{-/-}$ and counted.

Genomic DNA was then isolated from 1-5 million isolated PBMCs using the DNeasy Blood and Tissue kit (Qiagen; Cat. No. 69504) following manufacturer instructions. WES libraries were prepared using the SureSelect Human All Exon V8 Kit (Agilent; 5191-6873) and sequenced on either a NextSeq 2000 (Illumina) or NovaSeq 6000 (Illumina).

scRNA-seq and CITE-seq library preparation

Live CD45+ cells were used for scRNA sequencing after being FACS-enriched as described above. Cells that were used in CITE-seq experiments were blocked with TruStain Fc block (BioLegend; Cat. 422301) for 30 minutes. Cells were then incubated with TotalSeq B™ Universal cocktail (BioLegend; Cat. 399904) in Cell Staining Buffer (Biolegend; Cat. 420201) and washed following the manufacturer's protocol before being used for scRNA library preparation.

Cells isolated for scRNA/CITE-seq were suspended in ice-cold cell sorting buffer. scRNA GEMs and libraries were prepared according to the manufacturer's instructions. 5' libraries were prepared according to 10x Genomics CG000331 protocol, using Chromium Next GEM Single Cell 5' Kit v2 (10x Genomics; PN-1000263). 3' libraries were prepared using 10x Genomics CG000399 protocol, or CG000206 if a CITE-seq antibody panel was used with the appropriate 3' GEM kit (10x Genomics; PN 1000121). Both 3' and 5' libraries

used Dual Index Kit TT Set A (10x Genomics; PN 3000431). GEMs were created on either a Chromium Controller or Chromium X (10x Genomics). Either C1000 (Bio-rad) or SimpliAmp (Applied Biosystems) thermocyclers were used for library prep. Quality and concentrations of cDNA and final libraries were calculated from 2100 BioAnalyzer (Agilent) electrograms. Sequencing was performed on a NovaSeq 6000 (Ilumina).

Spatial transcriptomics

Biopsy tissues used for spatial transcriptomics were sectioned on a cryostat at 10 µm thickness and placed on Visium slides (10x Genomics; CG000239). Visium 3' libraries were prepared according to 10x Genomics Protocol CG000239 Rev G using a 30-minute incubation for tissue permeabilization. Either a C1000 (Bio-rad) or SimpliAmp (Applied Biosystems) thermocycler was used for library preparation. KAPA SYBR FAST qPCR Master Mix (2X) (Millipore Sigma; KK4600) and a QuantStudio 7 Pro qPCR (Applied Biosystems) were used to quantify cDNA following manufacturer recommendations. The Dual Index TT Set A (10x Genomics; PN 3000431) was used for the final library preparation and a 2100 Bioanalyzer (Agilent) was used to perform library quality control and concentration quantification. Sequencing was performed on a Novaseq 6000 (Ilumina).

Data analysis

Flow cytometry analysis: All data were analyzed with FlowJo™ software (v.10.8.1) (Becton, Dickinson, and Company; Ashland, OR, USA). Statistical analysis of flow data was performed with "stats" package in R (v.4.2.2) after importing into R. Functions used

for statistical testing included wilcox.test() and the additional following arguments “paired=TRUE” or “alternative = “less”” or “alternative = “greater”” for one-sided testing for unpaired data.

scRNA-Seq data processing and analysis: Reads from single-cell RNA-Seq experiments of each HC and UTx library were pre-processed and aligned against the GRCh38 human reference and quantified using Cell Ranger (v.6.1.1) from 10x Genomics. Downstream analysis of the generated Unique Molecular Identifier (UMI) count data was completed using R (v.4.2.1) and Seurat (v.4.4.0), utilizing default parameters unless otherwise specified. Prior to subsequent analyses, background noise from ambient RNA was removed using SoupX (v.1.6.2). The overall contamination fraction (rho) was parameterized using the autoEstCont function to remove > 2% background contamination in each dataset. The SoupX-corrected count matrixes were then loaded into R using the *Read10X* function from which Seurat objects were created per dataset via the *CreateSeuratObject* function. From each dataset, cells with less than 200 features, and features with less than 3 cells expressing them were filtered. Additionally, respective count matrixes were filtered based on quality control (QC) metrics and thresholds (table S3 and fig. S6). Doublets arising from the 10X sample loading procedure were detected and removed using Scrublet (v.0.2.3). The doublet rate per library was approximated using estimated rates provided by 10x Genomics.

Filtered count matrices were then merged into one Seurat object, normalized, and variance stabilized using regularized negative binomial regression via the *SCTransform*

package provided by Seurat (*77*). We also regressed out variation introduced by mitochondrial expression to prevent any confounding signal. Next, identification of principal components was performed using (RunPCA). Leveraging identified PCs, and while considering each individual library as a batch, the normalized dataset was corrected for batch effects and integrated using Harmony (v1.2.0). The resulting top 50 Harmony-corrected dimensions were further used to construct a k-nearest neighbor (KNN) graph using *FindNeighbors().* Cell clustering was subsequently performed using *FindClusters()* which employs a shared nearest neighbor (SNN) modularity optimization-based clustering algorithm. Resulting cluster information was used as input into the uniform manifold approximation and projection algorithm *RunUMAP()* which further aided the visualization of cell manifolds in a low-dimensional space. We ran Seurat's implementation of the Wilcoxon rank-sum test *FindMarkers()* to identify differentially expressed genes in each cluster. The expression of cluster-specific canonical markers was used to annotate each cell cluster.

CITE-Seq data processing and analysis of CD45+ endometrial immune cells

Three healthy control, and four uterine transplant datasets were further used for cell surface protein and transcriptomic data analyses. Pre-processing of these data was conducted as described previously. The RNA gene expression data was normalized using SCTransform (as earlier described), however, the ADT counts were centered log-ratio (CLR) normalized. Normalized ADT counts were then scaled and centered using the *ScaleData* function. Principal Component Analysis (PCA) was then conducted on both assays (RNA and ADT) using the *RunPCA* function with default parameters. We

leveraged the ElbowPlot and DimHeatmaps to determine the number of principal components (PCs) to consider for further downstream analyses. Towards cell clustering, we found the k-nearest neighbors of each cell using the Seurat *FindNeighbors* function which then constructed a shared nearest neighbor graph using the top 40 and top 20 dimensions for RNA and ADT assays respectively. As the data constitute multiple modalities, we leveraged Seurat's Version 4.4.0 to define cellular states based on these two assays. We applied the weighted-nearest neighbor (WNN) analysis (*78*), an unsupervised framework to integrate the multiple data types measured within each cell, and to obtain a unified definition of cellular state based on the multiple modalities. For each cell, a set of modality weights was learned, which reflects the relative information content for each data type in that cell. This enabled the generation of a WNN graph that denotes the most similar cells in the dataset based on a weighted combination of protein and RNA similarities. To achieve this, we used the Seurat *FindMultiModalNeighbors* function generating cell neighborhood graphs for further downstream analyses. We then preformed cell clustering on the generated graphs and identified clusters using the Louvain algorithm (*FindCluster* function) at the default resolution. We then utilized cluster information as input into the uniform manifold approximation and projection (*UMAP*) activated by the *RunUMAP* function which further aided the visualization of cell manifolds in a two-dimensional space, and as a weighted combination of RNA and protein data.

To identify differentially expressed (DE) genes between groups of cells, we used the *FindAllMarkers* function. Results from differential gene expression analysis were used to

annotate clusters based on the expression of top marker genes in the resulting clusters, and by leveraging feature plots (*FeaturePlot* function) of canonical cell type specific marker expression.

Module scores

Module scores were calculated using the *AddModuleScore()* function from Seurat. Respective feature plots were generated using *FeaturePlot()* with the features set as the calculated module scores from each gene program.

Identification of donor or recipient cellular origin in uterus transplant samples

To determine the identity of cells from uterus transplant recipients, we used sample-specific genetic mutations and Demuxlet (v.1.0-5) (*79*). Whole-exome sequencing (WES) was conducted on DNA isolated from donor and recipient PBMC samples collected prior to transplantation. Sequenced reads were aligned using STAR. Single nucleotide variants (SNVs) were detected using Freebayes (v.1.1.0-goolf-1.7.20_39e5e4b) for each donor and recipient sample. We provided a unique identifier per sample using “bcftools reheader” and filtered the resulting VCF files to retain only common SNPs with minor allele frequency (MAF) >= 0.05, and SNPs that overlap exons (defined by GENCODE release 19). The donor and recipient VCF files were then merged and sorted to match the recipient .BAM file from cellranger using popscle_helper_tools. Reads were piled up using the popscle dsc-pileup command using default parameters along with the filtered set of barcodes from cell ranger. The genetic deconvolution of sample identities in the UTx single-cell libraries was then conducted using Demuxlet (v.1.0-5) from the popscle

package by taking the merged donor and recipient .vcf file and the recipient .BAM file from Cell Ranger as inputs. Demuxlet was run at default parameters with the GT filed used to extract the genotype, likelihood, and posterior, and the offset of the genotype error rate (geno-error-offset) set to 0.05. Each cell in the final integrated dataset was annotated as donor or recipient using the BEST.GUESS column from the Demuxlet output data.

Cell2location

Visium spatial gene expression data processing and analysis using cell2location

i. Cell-type deconvolution of spatial transcriptomics data using cell2location (*60*).

To spatially resolve cell populations identified in healthy controls and uterine transplant biopsies, we used cell2location, a Bayesian model which estimates cell type abundance by deconvoluting a spatial expression count matrix into a set of reference cell type signatures. The model takes a spatial expression matrix with mRNA counts of genes at spatial locations and a matrix of reference cell type signatures as input. All cell2location analyses were conducted using Scanpy (v. 1.9) (*80*).

ii. Construction of scRNA-seq reference transcriptomes

Reference transcriptomes input into cell2location were derived from the sorted CD45+ immune cells from the six healthy control endometrial biopsies (scRNA-seq). These data were pre-processed as described above for scRNA-seq. The data were merged into a unified object using Seurat's merge function yielding a total of 41,719 cells and 20,636 genes in the reference dataset. The merged dataset was then normalized, scaled, and

variable features identified using the SCTransform() method in Seurat. Identification of principal components was performed using (RunPCA). Leveraging identified PCs, and while considering each individual library as a batch, the merged dataset was corrected for batch effects and integrated using Harmony (v1.2.0). Corrected Harmony embeddings (n=20) were further used to construct a k-nearest neighbor (KNN) graph using FindNeighbors. Clustering was subsequently performed using FindClusters which employs a shared nearest neighbor (SNN) modularity optimization-based clustering algorithm, resulting in 34 distinct reference cell clusters. Cluster information was used as input into the uniform manifold approximation and projection algorithm (RunUMAP) which further aided the visualization of cell manifolds in a low-dimensional space. We ran Seurat's implementation of the Wilcoxon rank-sum test (FindMarkers) to identify differentially expressed genes in each cluster. The expression of cluster-specific canonical markers was used to annotate each identified cell cluster (fig. S4).

iii. Estimating reference cell type signatures

The scRNA-seq reference data and corresponding reference cell type annotations were loaded into Scanpy using sc.read_10x_mtx. Gene selection and general QC were conducted as described before. Expression signatures of the 34 reference cell types in the reference dataset were then estimated using the negative binomial regression model while accounting for batch effects. The created model was further trained to estimate the reference cell type signatures on all cells in the dataset (train_size=1), mini-batch size = 2,500 and a training duration of 600 epochs, with GPU acceleration. Model accuracy was

evaluated based on the evidence lower bound (ELBO) loss and reconstruction accuracy plots.

iv. Spatial mapping of endometrial immune cell-types to spatially barcoded HC and UTx biopsies using cell2location

We imported the Visium spatial transcriptomics data for each biopsy from 10X Space Ranger into Scanpy, using scanpy.read_visium. Mitochondrial genes were identified and removed. Before running cell2location to map our reference cell types to each Visium dataset, both the estimated reference cell type signatures (gene expression), and spatial data from each respective biopsy were filtered to select genes shared between the two data objects. The filtered objects were both used as input to cell2location. We specified two hyperparameters required to run cell2location: 1) The expected cell abundance per location (N_cells_per_location), which was estimated by manually counting cells in 10 random capture spots from the respective H&E images and averaging these values to give us the average cell abundance per tissue sample (HC = 14.5 cells/capture spot; UTx = 17.7 cells/capture spot); and 2) a parameter which accounted for within-experiment variation in RNA detection sensitivity (detection_alpha). We set detection alpha = 20 in order to ensure the greatest accuracy and sensitivity given that strong gradients in mRNA detection sensitivity are commonly observed in adult human 10x Visium data.

After providing the reference cell type signatures, spatial data, and hyperparameters specified above as inputs, the cell2location model was trained using max_epochs = 30000 on the full dataset (batch_size = None) while estimating cell abundance at all

locations (train_size = 1). We plotted ELBO loss history during training and assessed mapping quality by examining reconstruction accuracy plots. We exported estimated posterior distributions of cell abundance ('num_samples': 1000, 'batch_size': mod.adata.n_obs, 'use_gpu': True) and added a 5% quantile of the posterior distribution, representing the value of cell abundance corresponding to high confidence in the model. We further leveraged Scanpy's plotting function scanpy.pl.spatial to visualize spatial scatter plots of cell type abundance in spatial coordinates.

<u>Spatially barcoded libraries prepared from one healthy control and one uterine transplant endometrial biopsy.</u>

i. Data pre-processing

Base call (BCL) files were converted to FASTQ files using the Space Ranger (v.1.3.1) mkfastq function. Space Ranger count function was used to align the FASTQ files to the human reference genome GRCh38 to generate count matrices.

Gene set enrichment analysis Gene set enrichment analysis was performed using the FGSEA package. Inputs included gene sets of interest and ranked differentially expressed gene lists created with MAST (*81*) and the Seurat *Findmarkers()* function. Resulting differentially expressed genes were ranked based on the log-fold change (or a combinatory metric of absolute log-fold change * log transformed p-values) and the ranked gene list used as input for the fgsea R package (fast preranked GSEA), with a minimum set size of 15 genes and a maximum of 500 genes. We used the plotEnrichment() function to visualize the resulting gene set enrichment.

Manual curation of NFAT-dependent genes A set of NFAT dependent genes was manually curated through literature review as well as analysis of publicly available data from NFAT-deficient mice.

Placental Histopathology

H&E-stained slides of the placental disk were evaluated by an experienced perinatal pathologist (V.E.D.). Placental lesions were identified according to the criteria established by the Amsterdam Placental Workshop Group Consensus (*82*) and tissue was processed according to standard laboratory protocols. Placental density was calculated using automated image analysis as previously described (*83*).

Immunofluorescence microscopy

Fresh frozen biopsies in OCT compound (Tissue-Tek) were sectioned on a cryostat at 20 mm thickness and placed on Superfrost Plus slides (Fisher) for processing. Slides were placed in 4% formaldehyde in phosphate buffered saline (PBS), pre-chilled to 4°C, for 30 minutes, then washed in PBS plus 0.3% Tween 20 three times for five minutes per wash at room temperature (RT). Slides were then dried for 15 min at RT, and sections were then treated with blocking buffer (PBS plus 1% Triton X-100, 1% normal goat serum, 1% bovine serum albumin) at RT for 1hr. Primary antibodies (rabbit anti-human NCAM1 (CD56), Cell Signaling Tech. 99746T; hamster anti-human CD3e, BioLegend 100302) were diluted (CD56: 1:50; CD3: 1:200) in blocking buffer and applied overnight at 4°C. Sections were washed in PBST three times (five minutes per wash), then treated with

fluorophore-conjugated secondary antibody (donkey anti-rabbit IgG Alexa Fluor 488, Invitrogen A32790TR; goat anti-hamster IgG Alexa Fluor 594, BioLegend B388503) diluted 1:1000 in blocking buffer for 1hr at RT. Sections were then washed three times in PBST, five min per wash, then treated with DAPI (Invitrogen 62248) diluted 1:1000 in PBST for 1.5min at RT, washed once in PBST, mounted in Prolong Diamond under coverglass No. 1.5 and allowed to cure overnight. Images were obtained on ECHO Revolution in upright mode using a 20x PLAN X Apo 0.8 NA objective and a 5MP 12bit monochrome CMOS camera. Each imaged field consists of a 2416x2016 pixel array with pixel physical dimensions of 0.1777x0.1777 mm and each field covering 0.15 mm^2 of tissue.

Image analysis and error estimation

Raw tagged image files were processed with custom software written in MATLAB. The analysis consisted of identifying centroids representing the centers of nuclei from the DAPI channel, then assigning cells of positive or negative CD56 or CD3 expression to each centroid. This assignment was based on relative signal in the CD56 or CD3 channel in pixels near each centroid within DAPI-based masks created as described here.

Nucleus centroid positions were estimated by a combination of iterative thresholding, difference-of-Gaussian (DoG) filtering, and iterative erosion. Single image fields were initially filtered with a Gaussian of radius 1.25 pixels, then corrected for local background changes by top-hat filtering with a disk-shaped structuring element with a 50 pixel radius. The resulting image was filtered with a disk-shaped structuring element of 0.9 pixel radius.

On the resulting image, we performed iterative thresholding to find candidate "connected component" objects potentially representing single isolated nuclei or multiple overlaying nuclei. Objects whose area spanned the range of nucleus sizes determined empirically (covering between 500 and 6000 pixels) and with a circularity (calculated as four times the Area times pi divided by the perimeter) greater than 0.85 were retained as representing single nuclei. Noncircular objects were subject to iterative erosion with either a square structuring element or a diamond structuring element until either the object was divided into two or more objects, in which case two or more new centroids were taken as representing single nuclei, or the object disappeared entirely, in which case the original object was kept as a nucleus. Objects larger than 6000 pixels were subsequently processed by isolating each object's bounding box from the filtered image and replacing all pixels outside the object with zeros. This object-specific snippet was then processed by DoG filtering with Gaussians of 10 and 12 radii. The filtered image was binarized, morphologically closed, and subjected to the same size and circularity selection criteria already described. This process was performed iteratively to subdivide all large objects into candidate nucleus objects with the selected size specificities. Centroids were then generated from all the candidate objects discovered by this method. A watershed was then applied to the original connected component mask to assign pixels to the nearest centroid. To call each centroid as expressing CD56 or CD3, the mean intensity in the CD56 or CD3 channel was assessed over all pixels assigned to each centroid after filtering with a Gaussian of radius 15 pixels. Threshold selection was performed by finding the inflection point in the rate of increase in the fraction of centroids called positive as a function of candidate threshold level.

For error estimation, we compared the computer performance to that of imaging specialists in a set of ten test images each covering 12,500 mm^2 and containing an average of 130±33 (mean ± s.d.) hand-counted nuclei, for a total of 1,295 nuclei spanning a range of densities. Using hand-selected nuclei as the gold standard, we noted four types of error, two related to nuclear segmentation and two for assigning CD56 expression status: 1) failure to detect a nucleus, usually as a result of incorrectly merging multiple nuclei into a single nucleus; 2) counting excess nuclei, usually as a result of merging of multiple nuclei into a single nucleus; 3) incorrect splitting of single nuclei; 4) failure to call a CD56+ nucleus; 5) incorrectly calling a negative nucleus as positive. To calculate (1) and (2), we generated unique nearest-neighbor pairs of hand-selected and computer-generated centroids while using an exclusion rule prohibiting pairing of centroids separated by more than the average diameter of well-separated nuclei (8 mm). We thereby generated lists of unpaired hand-selected and unpaired computer-generated centroids and calculated the fraction of the total. Errors (3) and (4) were calculated by assessing the fraction of positive (or negative) nuclei that the computer called as negative (or positive) out of the successfully paired set of nuclei. The estimated rate for each error is 0.053±0.029, 0.051±0.043, 0.026±0.013, 0.024±0.015 (mean ± SEM). Assuming these errors arise independently, the total uncertainty in the fraction of CD56+ nuclei may be calculated by finding the root of the sum of the squares of the errors. The estimated uncertainty is thus about 8% and may be as high as 11% (0.082±0.030). Using this upper estimate, the mean fraction of cells that are CD56+ in the healthy control biopsies are

0.0303±0.0033 and 0.0357±0.0039, whereas the transplant biopsies have fractions of 0.0181±0.002, 0.0286±0.0031, 0.0125±0.0014, and 0.0122±0.0013.

LIST OF SUPPLEMENTARY MATERIALS

Figs. S1-S6

Tables S1-S3

REFERENCES AND NOTES

1. S. E. Ander, M. S. Diamond, C. B. Coyne, Immune responses at the maternal-fetal interface. *Sci Immunol* **4**, (2019).
2. M. PrabhuDas *et al.*, Immune mechanisms at the maternal-fetal interface: perspectives and challenges. *Nat Immunol* **16**, 328-334 (2015).
3. B. Fu *et al.*, Natural Killer Cells Promote Fetal Development through the Secretion of Growth-Promoting Factors. *Immunity* **47**, 1100-1113 e1106 (2017).
4. Y. Zhou *et al.*, PBX1 expression in uterine natural killer cells drives fetal growth. *Sci Transl Med* **12**, (2020).
5. Q. Li *et al.*, Human uterine natural killer cells regulate differentiation of extravillous trophoblast early in pregnancy. *Cell Stem Cell* **31**, 181-195 e189 (2024).
6. E. D. Albrecht, G. J. Pepe, Regulation of Uterine Spiral Artery Remodeling: a Review. *Reprod Sci* **27**, 1932-1942 (2020).
7. A. A. Ashkar, J. P. Di Santo, B. A. Croy, Interferon gamma contributes to initiation of uterine vascular modification, decidual integrity, and uterine natural killer cell maturation during normal murine pregnancy. *J Exp Med* **192**, 259-270 (2000).

8. J. E. Cartwright, R. Fraser, K. Leslie, A. E. Wallace, J. L. James, Remodelling at the maternal-fetal interface: relevance to human pregnancy disorders. *Reproduction* **140**, 803-813 (2010).

9. C. M. Craven, T. Morgan, K. Ward, Decidual spiral artery remodelling begins before cellular interaction with cytotrophoblasts. *Placenta* **19**, 241-252 (1998).

10. B. A. Croy *et al.*, Imaging of vascular development in early mouse decidua and its association with leukocytes and trophoblasts. *Biol Reprod* **87**, 125 (2012).

11. Y. Cui *et al.*, Role of corin in trophoblast invasion and uterine spiral artery remodelling in pregnancy. *Nature* **484**, 246-250 (2012).

12. A. M. Felker, B. A. Croy, Natural cytotoxicity receptor 1 in mouse uNK cell maturation and function. *Mucosal Immunol* **10**, 1122-1132 (2017).

13. M. J. Guimond, B. Wang, B. A. Croy, Engraftment of bone marrow from severe combined immunodeficient (SCID) mice reverses the reproductive deficits in natural killer cell-deficient tg epsilon 26 mice. *J Exp Med* **187**, 217-223 (1998).

14. J. Hanna *et al.*, Decidual NK cells regulate key developmental processes at the human fetal-maternal interface. *Nat Med* **12**, 1065-1074 (2006).

15. A. D. Hazan *et al.*, Vascular-leukocyte interactions: mechanisms of human decidual spiral artery remodeling in vitro. *Am J Pathol* **177**, 1017-1030 (2010).

16. J. Kieckbusch, L. M. Gaynor, A. Moffett, F. Colucci, MHC-dependent inhibition of uterine NK cells impedes fetal growth and decidual vascular remodelling. *Nat Commun* **5**, 3359 (2014).

17. G. E. Lash *et al.*, Expression of angiogenic growth factors by uterine natural killer cells during early pregnancy. *J Leukoc Biol* **80**, 572-580 (2006).

18. P. D. Lima, J. Zhang, C. Dunk, S. J. Lye, B. A. Croy, Leukocyte driven-decidual angiogenesis in early pregnancy. *Cell Mol Immunol* **11**, 522-537 (2014).

19. A. Robson *et al.*, Uterine natural killer cells initiate spiral artery remodeling in human pregnancy. *FASEB J* **26**, 4876-4885 (2012).

20. A. Robson *et al.*, Uterine spiral artery muscle dedifferentiation. *Hum Reprod* **34**, 1428-1438 (2019).

21. S. D. Smith, C. E. Dunk, J. D. Aplin, L. K. Harris, R. L. Jones, Evidence for immune cell involvement in decidual spiral arteriole remodeling in early human pregnancy. *Am J Pathol* **174**, 1959-1971 (2009).

22. W. Zhang *et al.*, Atrial natriuretic peptide promotes uterine decidualization and a TRAIL-dependent mechanism in spiral artery remodeling. *J Clin Invest* **131**, (2021).

23. A. C. Staff *et al.*, Failure of physiological transformation and spiral artery atherosis: their roles in preeclampsia. *Am J Obstet Gynecol* **226**, S895-S906 (2022).

24. N. Shreeve *et al.*, The CD94/NKG2A inhibitory receptor educates uterine NK cells to optimize pregnancy outcomes in humans and mice. *Immunity* **54**, 1231-1244 e1234 (2021).

25. I. Brosens, R. Pijnenborg, L. Vercruysse, R. Romero, The "Great Obstetrical Syndromes" are associated with disorders of deep placentation. *Am J Obstet Gynecol* **204**, 193-201 (2011).

26. C. A. Labarrere *et al.*, Failure of physiologic transformation of spiral arteries, endothelial and trophoblast cell activation, and acute atherosis in the basal plate of the placenta. *Am J Obstet Gynecol* **216**, 287 e281-287 e216 (2017).

27. C. Guo *et al.*, Single-cell profiling of the human decidual immune microenvironment in patients with recurrent pregnancy loss. *Cell Discov* **7**, 1 (2021).

28. B. Strunz *et al.*, Continuous human uterine NK cell differentiation in response to endometrial regeneration and pregnancy. *Sci Immunol* **6**, (2021).

29. C. Dominguez Conde *et al.*, Cross-tissue immune cell analysis reveals tissue-specific features in humans. *Science* **376**, eabl5197 (2022).

30. J. I. Gray, D. L. Farber, Tissue-Resident Immune Cells in Humans. *Annu Rev Immunol* **40**, 195-220 (2022).

31. N. Marquardt *et al.*, Unique transcriptional and protein-expression signature in human lung tissue-resident NK cells. *Nat Commun* **10**, 3841 (2019).

32. M. M. L. Poon *et al.*, Tissue adaptation and clonal segregation of human memory T cells in barrier sites. *Nat Immunol* **24**, 309-319 (2023).

33. P. A. Szabo *et al.*, Single-cell transcriptomics of human T cells reveals tissue and activation signatures in health and disease. *Nat Commun* **10**, 4706 (2019).

34. T. J. Kim *et al.*, FK506 causes cellular and functional defects in human natural killer cells. *J Leukoc Biol* **88**, 1089-1097 (2010).

35. H. Wang *et al.*, The unexpected effect of cyclosporin A on CD56+CD16- and CD56+CD16+ natural killer cell subpopulations. *Blood* **110**, 1530-1539 (2007).

36. N. A. Deshpande *et al.*, Pregnancy outcomes of liver transplant recipients: a systematic review and meta-analysis. *Liver Transpl* **18**, 621-629 (2012).

37. N. A. Deshpande *et al.*, Pregnancy outcomes in kidney transplant recipients: a systematic review and meta-analysis. *Am J Transplant* **11**, 2388-2404 (2011).

38. N. Jha, A. K. Jha, S. K. Mishra, S. Parida, Thoracic organ transplantation and pregnancy outcomes: systematic review and meta-analysis. *Arch Gynecol Obstet* **309**, 385-396 (2024).

39. A. Lauro, C. S. Matsumoto, I. R. Marino, V. Berghella, A review on pregnancy after intestinal transplantation. *J Matern Fetal Neonatal Med* **30**, 205-212 (2017).

40. Z. Stanic *et al.*, Successful spontaneous pregnancy after simultaneous kidney and pancreas transplant. *Int J Gynaecol Obstet* **162**, 773-774 (2023).

41. O. Yin *et al.*, Mode of Obstetric Delivery in Kidney and Liver Transplant Recipients and Associated Maternal, Neonatal, and Graft Morbidity During 5 Decades of Clinical Practice. *JAMA Netw Open* **4**, e2127378 (2021).

42. I. Brosens, J. J. Brosens, G. Benagiano, The risk of obstetrical syndromes after solid organ transplantation. *Best Pract Res Clin Obstet Gynaecol* **28**, 1211-1221 (2014).

43. D. B. McKay *et al.*, Reproduction and pregnancy in transplant recipients: current practices. *Prog Transplant* **16**, 127-132 (2006).

44. D. M. Rupley *et al.*, Preconception counseling, fertility, and pregnancy complications after abdominal organ transplantation: a survey and cohort study of 532 recipients. *Clin Transplant* **28**, 937-945 (2014).

45. L. Johannesson *et al.*, The First 5 Years of Uterus Transplant in the US: A Report From the United States Uterus Transplant Consortium. *JAMA Surg* **157**, 790-797 (2022).

46. B. P. Jones *et al.*, Human uterine transplantation: a review of outcomes from the first 45 cases. *BJOG* **126**, 1310-1319 (2019).

47. D. Sawinski *et al.*, A multi-institutional study of renal outcomes and renal-related pregnancy outcomes in uterus transplant recipients. *Am J Transplant* **22**, 3101-3110 (2022).

48. A. King, V. Wellings, L. Gardner, Y. W. Loke, Immunocytochemical characterization of the unusual large granular lymphocytes in human endometrium throughout the menstrual cycle. *Hum Immunol* **24**, 195-205 (1989).

49. M. J. van den Heuvel *et al.*, Menstrual cycle hormones induce changes in functional interactions between lymphocytes and decidual vascular endothelial cells. *J Clin Endocrinol Metab* **90**, 2835-2842 (2005).

50. I. Korsunsky *et al.*, Fast, sensitive and accurate integration of single-cell data with Harmony. *Nat Methods* **16**, 1289-1296 (2019).

51. L. M. Ernst, Maternal vascular malperfusion of the placental bed. *APMIS* **126**, 551-560 (2018).

52. Y. M. Kim *et al.*, Failure of physiologic transformation of the spiral arteries in the placental bed in preterm premature rupture of membranes. *Am J Obstet Gynecol* **187**, 1137-1142 (2002).

53. W. T. Parks, J. M. Catov, The Placenta as a Window to Maternal Vascular Health. *Obstet Gynecol Clin North Am* **47**, 17-28 (2020).

54. M. Eriksson, S. K. Meadows, C. R. Wira, C. L. Sentman, Unique phenotype of human uterine NK cells and their regulation by endogenous TGF-beta. *J Leukoc Biol* **76**, 667-675 (2004).

55. E. Giuliani, K. L. Parkin, B. A. Lessey, S. L. Young, A. T. Fazleabas, Characterization of uterine NK cells in women with infertility or recurrent pregnancy loss and associated endometriosis. *Am J Reprod Immunol* **72**, 262-269 (2014).

56. M. Greene *et al.*, Sequential transcriptional programs of tissue residency drive human uterine NK cell development. *bioRxiv* **https://doi.org/10.1101/2024.02.29.582684**, (2024).

57. P. Dogra *et al.*, Tissue Determinants of Human NK Cell Development, Function, and Residence. *Cell* **180**, 749-763 e713 (2020).

58. L. Kok, D. Masopust, T. N. Schumacher, The precursors of CD8(+) tissue resident memory T cells: from lymphoid organs to infected tissues. *Nat Rev Immunol* **22**, 283-293 (2022).

59. O. Huhn *et al.*, Distinctive phenotypes and functions of innate lymphoid cells in human decidua during early pregnancy. *Nat Commun* **11**, 381 (2020).

60. R. Vento-Tormo *et al.*, Single-cell reconstruction of the early maternal-fetal interface in humans. *Nature* **563**, 347-353 (2018).

61. V. Kleshchevnikov *et al.*, Cell2location maps fine-grained cell types in spatial transcriptomics. *Nat Biotechnol* **40**, 661-671 (2022).

62. L. K. Mackay *et al.*, The developmental pathway for CD103(+)CD8+ tissue-resident memory T cells of skin. *Nat Immunol* **14**, 1294-1301 (2013).

63. L. K. Mackay *et al.*, T-box Transcription Factors Combine with the Cytokines TGF-beta and IL-15 to Control Tissue-Resident Memory T Cell Fate. *Immunity* **43**, 1101-1111 (2015).

64. A. P. Nath *et al.*, Comparative analysis reveals a role for TGF-beta in shaping the residency-related transcriptional signature in tissue-resident memory CD8+ T cells. *PLoS One* **14**, e0210495 (2019).

65. N. S. Kurd *et al.*, Early precursors and molecular determinants of tissue-resident memory CD8(+) T lymphocytes revealed by single-cell RNA sequencing. *Sci Immunol* **5**, (2020).

66. M. Mokrani, J. Klibi, D. Bluteau, G. Bismuth, F. Mami-Chouaib, Smad and NFAT pathways cooperate to induce CD103 expression in human CD8 T lymphocytes. *J Immunol* **192**, 2471-2479 (2014).

67. J. J. Milner *et al.*, Runx3 programs CD8(+) T cell residency in non-lymphoid tissues and tumours. *Nature* **552**, 253-257 (2017).

68. G. P. Mognol, F. R. Carneiro, B. K. Robbs, D. V. Faget, J. P. Viola, Cell cycle and apoptosis regulation by NFAT transcription factors: new roles for an old player. *Cell Death Dis* **7**, e2199 (2016).

69. J. Fric *et al.*, NFAT control of innate immunity. *Blood* **120**, 1380-1389 (2012).

70. J. Barlic *et al.*, Interleukin (IL)-15 and IL-2 reciprocally regulate expression of the chemokine receptor CX3CR1 through selective NFAT1- and NFAT2-dependent mechanisms. *J Biol Chem* **279**, 48520-48534 (2004).

71. L. G. Hawke, B. Z. Mitchell, M. L. Ormiston, TGF-beta and IL-15 Synergize through MAPK Pathways to Drive the Conversion of Human NK Cells to an Innate Lymphoid Cell 1-like Phenotype. *J Immunol* **204**, 3171-3181 (2020).

72. M. J. Shannon, E. M. Mace, Natural Killer Cell Integrins and Their Functions in Tissue Residency. *Front Immunol* **12**, 647358 (2021).

73. S. Klein-Hessling *et al.*, NFATc1 controls the cytotoxicity of CD8(+) T cells. *Nat Commun* **8**, 511 (2017).

74. K. Kitaya *et al.*, IL-15 expression at human endometrium and decidua. *Biol Reprod* **63**, 683-687 (2000).

75. W. Wang *et al.*, Single-cell transcriptomic atlas of the human endometrium during the menstrual cycle. *Nat Med* **26**, 1644-1653 (2020).

76. C. C. Wu, S. C. Hsu, H. M. Shih, M. Z. Lai, Nuclear factor of activated T cells c is a target of p38 mitogen-activated protein kinase in T cells. *Mol Cell Biol* **23**, 6442-6454 (2003).

77. C. Hafemeister, R. Satija, Normalization and variance stabilization of single-cell RNA-seq data using regularized negative binomial regression. *Genome Biol* **20**, 296 (2019).

78. Y. Hao *et al.*, Integrated analysis of multimodal single-cell data. *Cell* **184**, 3573-3587 e3529 (2021).

79. H. M. Kang *et al.*, Multiplexed droplet single-cell RNA-sequencing using natural genetic variation. *Nat Biotechnol* **36**, 89-94 (2018).

80. F. A. Wolf, P. Angerer, F. J. Theis, SCANPY: large-scale single-cell gene expression data analysis. *Genome Biol* **19**, 15 (2018).

81. G. Finak *et al.*, MAST: a flexible statistical framework for assessing transcriptional changes and characterizing heterogeneity in single-cell RNA sequencing data. *Genome Biol* **16**, 278 (2015).

82. T. Y. Khong *et al.*, Sampling and Definitions of Placental Lesions: Amsterdam Placental Workshop Group Consensus Statement. *Arch Pathol Lab Med* **140**, 698-713 (2016).

83. D. Kidron, I. Vainer, Y. Fisher, R. Sharony, Automated image analysis of placental villi and syncytial knots in histological sections. *Placenta* **53**, 113-118 (2017).

ACKNOWLEDGEMENTS

The authors would like to thank the following individuals and organizations for their following contributions to this work:

1) Legacy of Hope Organ Procurement Organization
2) Uterus transplant clinical care team at the University of Alabama at Birmingham
3) Staff at the UAB flow cytometry and single cell core facilities
4) Mr. Reid Jones for support of the UAB uterus transplant program

Funding

This work was supported by a pilot grant from the UAB Center for Women's Reproductive Health (to P.M.P.); UAB AMC21 grants (to J.E.L., J.F.G., & P.M.P.); and start-up funding from the UAB Heersink School of Medicine (to P.M.P.). Salary support was provided by R01AI145905 (to P.M.P.); R01CA208353 (to A.G.F. and P.M.P.); American Cancer Society Research Scholar Grant #RSG-23-1153857-01-IBCD (to A.G.F.).

Author Contributions

R.A.: data curation, analysis, visualization, software.

B.K.: data analysis; writing – original draft; conceptualization.

M.E.G.: investigation; data analysis, conceptualization.

E.W., M.B., D.E., S.D.Y., M.D.C., R.B., N.A., V.E.D., H.E.R., D.G.: investigation, methodology.

J.E.L.: resources, funding acquisition.

M.V.G.: data analysis, conceptualization.

S.F., E.B., and S.C.: project administration.

J.F.G.: resources, supervision, funding acquisition.

A.G.F.: conceptualization.

S.C.L.: conceptualization, supervision, data analysis, data curation, investigation, visualizations, writing – original draft, software.

P.M.P.: conceptualization, supervision, data analysis, visualizations, writing – original draft, funding acquisition.

All authors: writing – review and editing.

Competing Interests: The authors have no competing interests to declare.

Data & Code Availability

Raw FASTQ files have been deposited to NCBI GEO under accession number GSEXXXXXX.

Additional data are available upon request from the corresponding author.

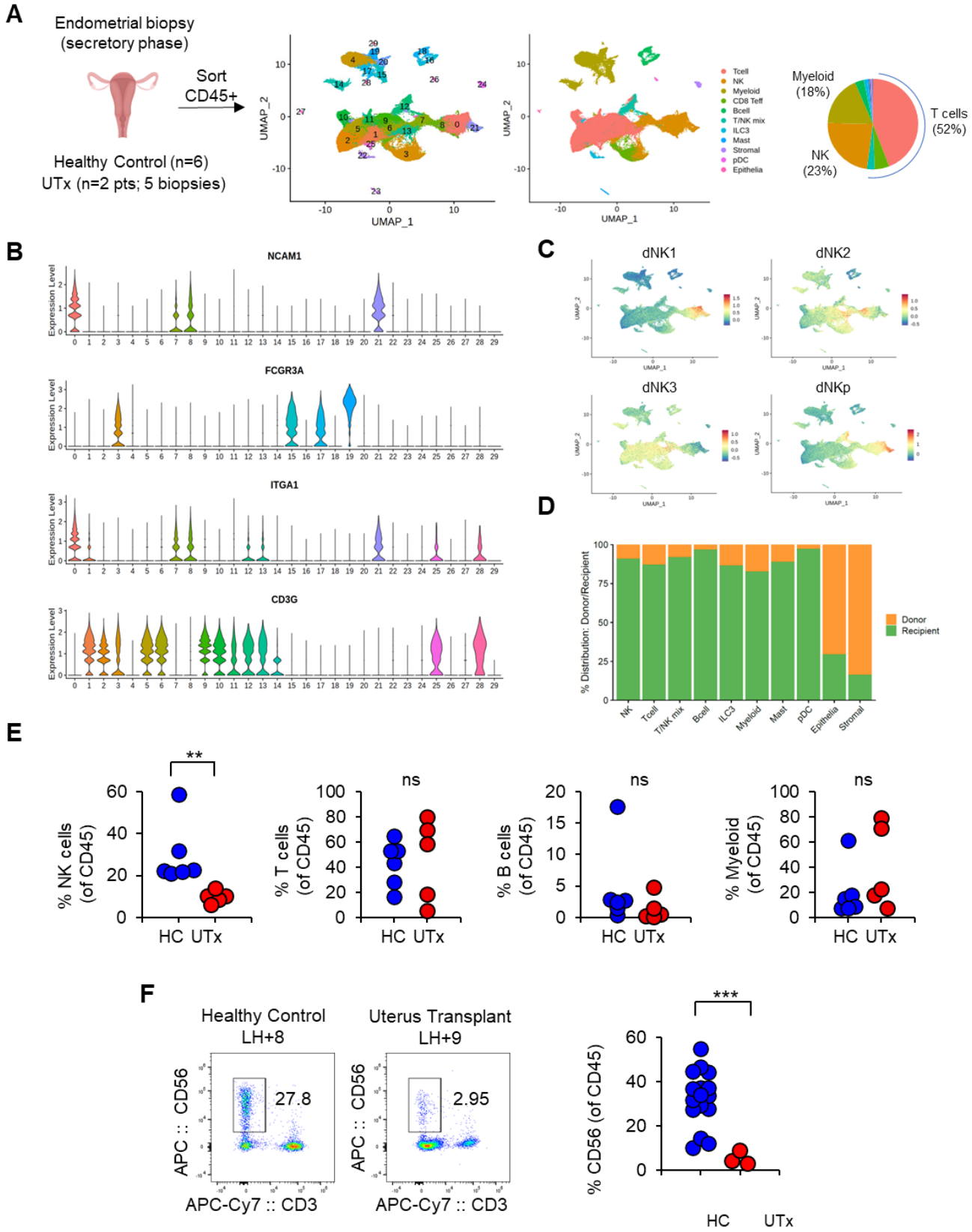
A
Endometrial biopsy
(secretory phase)
Sort
CD45+
Healthy Control (n=6)
UTx (n=2 pts; 5 biopsies)
UMAP_1
UMAP_2
Tcell
NK
Myeloid
CD8 Teff
Bcell
T/NK mix
ILC3
Mast
Stromal
pDC
Epithelia
Myeloid
(18%)
T cells
(52%)
NK
(23%)
B
NCAM1
FCGR3A
ITGA1
CD3G
Expression Level
C
dNK1
dNK2
dNK3
dNKp
D
% Distribution: Donor/Recipient
Donor
Recipient
NK
Tcell
T/NK mix
Bcell
ILC3
Myeloid
Mast
pDC
Epithelia
Stromal
E
**
ns
ns
ns
% NK cells
(of CD45)
% T cells
(of CD45)
% B cells
(of CD45)
% Myeloid
(of CD45)
HC
UTx
F
Healthy Control
LH+8
Uterus Transplant
LH+9
27.8
2.95
APC :: CD56
APC-Cy7 :: CD3
***
% CD56 (of CD45)
HC
UTx

Fig. 1

Figure 1. Reduced NK cell frequency among UTx endometrial immune cells. (**A**) UMAP visualization of broad and fine immune clusters among secretory phase endometrial biopsies from healthy control volunteers (n=6) (HC) and uterus transplant recipients (n=5) (UTx). Contaminating stromal and epithelial cells are also shown. (n=77,481 total cells) (**B**) Expression of major cell-type specific marker genes among CD45+ immune cells. (**C**) Module scores of decidual NK cell transcriptomes. (**D**) Frequence of donor-derived (yellow) or recipient-derived (green) cells in each cluster. (**E**) NK cells are reduced in frequency among sequenced CD45+ immune cells in human endometrium. **P<0.01; Mann Whitney U test (one-tailed). ns=not significant. (**F**) Flow cytometric analysis was performed in parallel on three UTx secretory phase biopsies and an expanded cohort of HCs (n=16). Bivariate plots are representative data. Plots are gated on live, CD45+ singlets. **P<0.01; Mann Whitney U test (one-tailed).

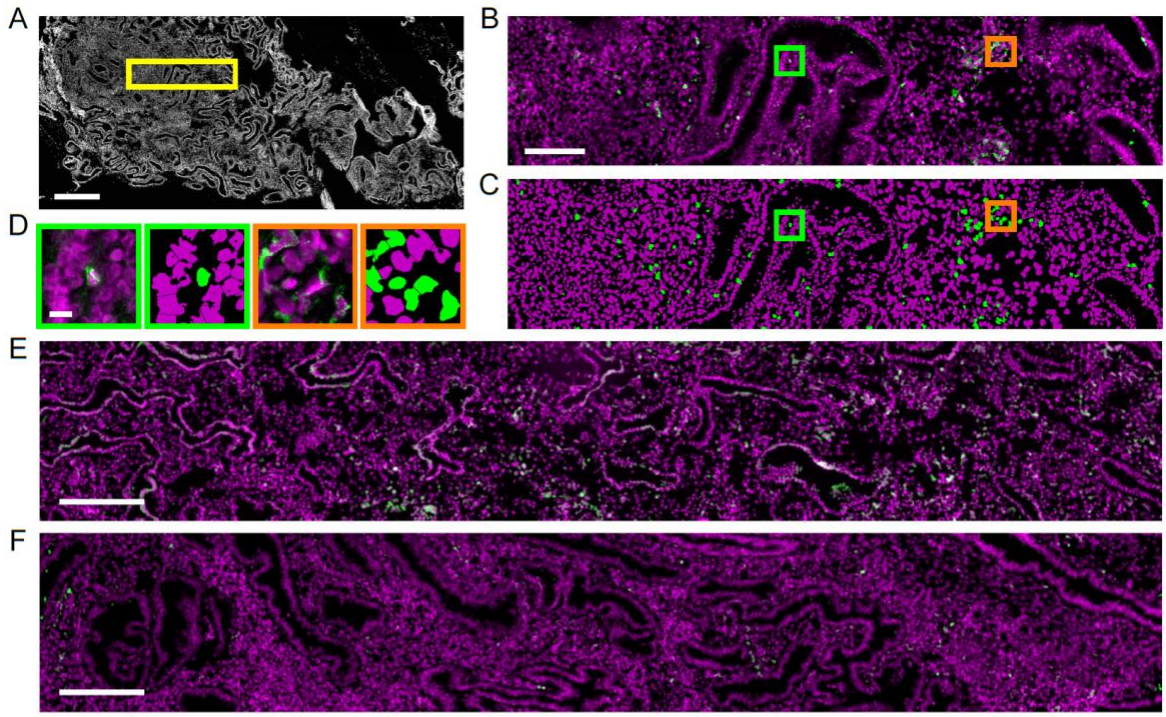

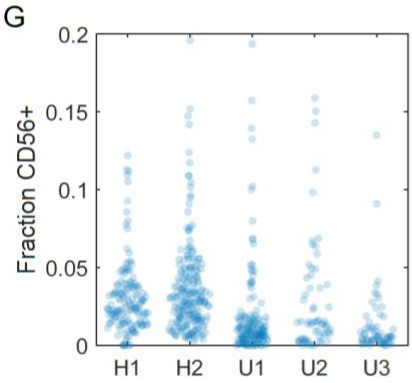

H

	H1	H2	U1	U2	U3
mean	0.0303	0.0357	0.0181	0.0286	0.0125
median	0.0243	0.0285	0.0090	0.0142	0.0054
SD	0.0231	0.0293	0.0294	0.0370	0.0214
# cells	135417	197679	122635	42871	48208
# fields	143	204	149	62	62

I

Mann-Whitney U test

	H2	U1	U2	U3
H1	0.0136	8.96E-12	0.0984	7.93E-08
H2		3.11E-18	0.0019	1.87E-11
U1			0.0164	0.257
U2				0.0132

Fig. 2

Figure 2. CD56+ cells are reduced in endometrial tissue sections of transplanted uteri. (**A**) Low-magnification DAPI channel from fluorescence microscopy of healthy control endometrial biopsy ("H1" in panels G-I). Box (yellow) indicates area shown in panel B. (**B**) High magnification image showing DAPI (magenta) and anti-CD56 staining (green). (**C**) Computerized rendering of panel B showing CD56+ (green) and CD56- (magenta) nuclei. Boxes indicate areas shown in D. (**D**) Data (left) and computer rendering (right) of the green and orange boxed areas shown in B and C. (**E** and **F**) DAPI (magenta) and anti-CD56 (green) staining in a second control biopsy (E) and a biopsy taken 57 days after uterus transplant (F), designated "H2" and "U1", respectively, in panels G-I. (**G**) Fraction of nuclei designated CD56+ in two healthy control (H1 and H2) and three uterus transplant biopsies (U1-U3). Data points represent individual 0.15 mm2 imaging fields. (**H**) Summary statistics for the five biopsies. (**I**) p-values (Mann-Whitney U test) for all pairwise comparisons of the five biopsies. Scale bars: 500 µm (A), 100 µm (B), 10 µm (D), 200 µm (E,F). See table S1 for additional details regarding samples.

A

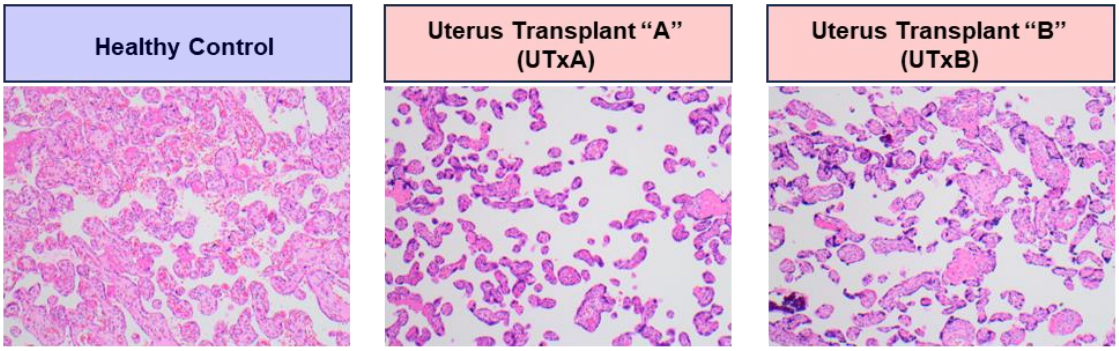
Healthy Control
Uterus Transplant "A" (UTxA)
Uterus Transplant "B" (UTxB)

B

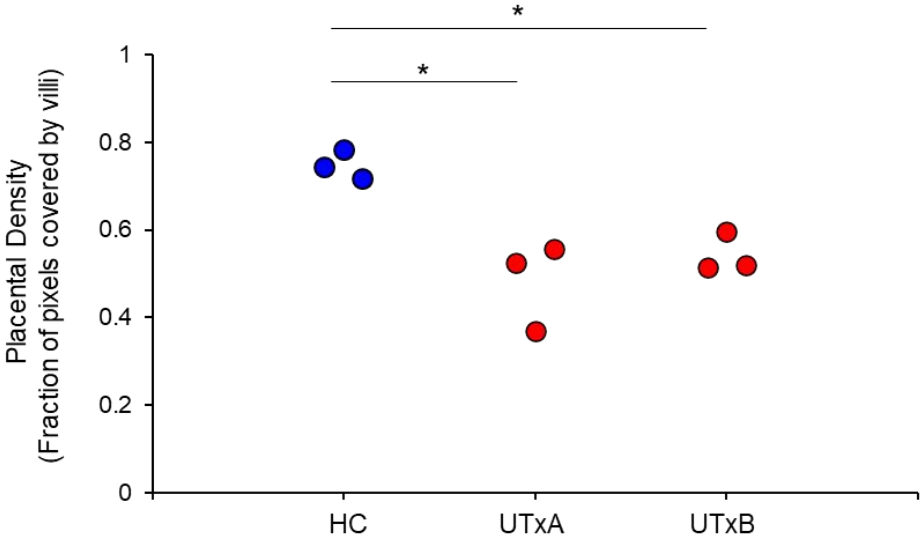
*
*
Placental Density
(Fraction of pixels covered by villi)
1
0.8
0.6
0.4
0.2
0
HC
UTxA
UTxB

Fig. 3

Figure 3. Maternal vascular malperfusion in UTx placentas. (**A**) UTx "A" and UTx "B" show regions of distal villi that are sparsely distributed, markedly smaller in caliber, show less branching, and have increased numbers of syncytial knots relative to a control placenta (HC) from a similar gestational age. H&E 10X. Gestational age = 34 weeks for all micrographs. (**B**) Density of villi is plotted for each sample as shown. Individual data points represent technical replicates. *P=0.05; one-sided Mann Whitney U test.

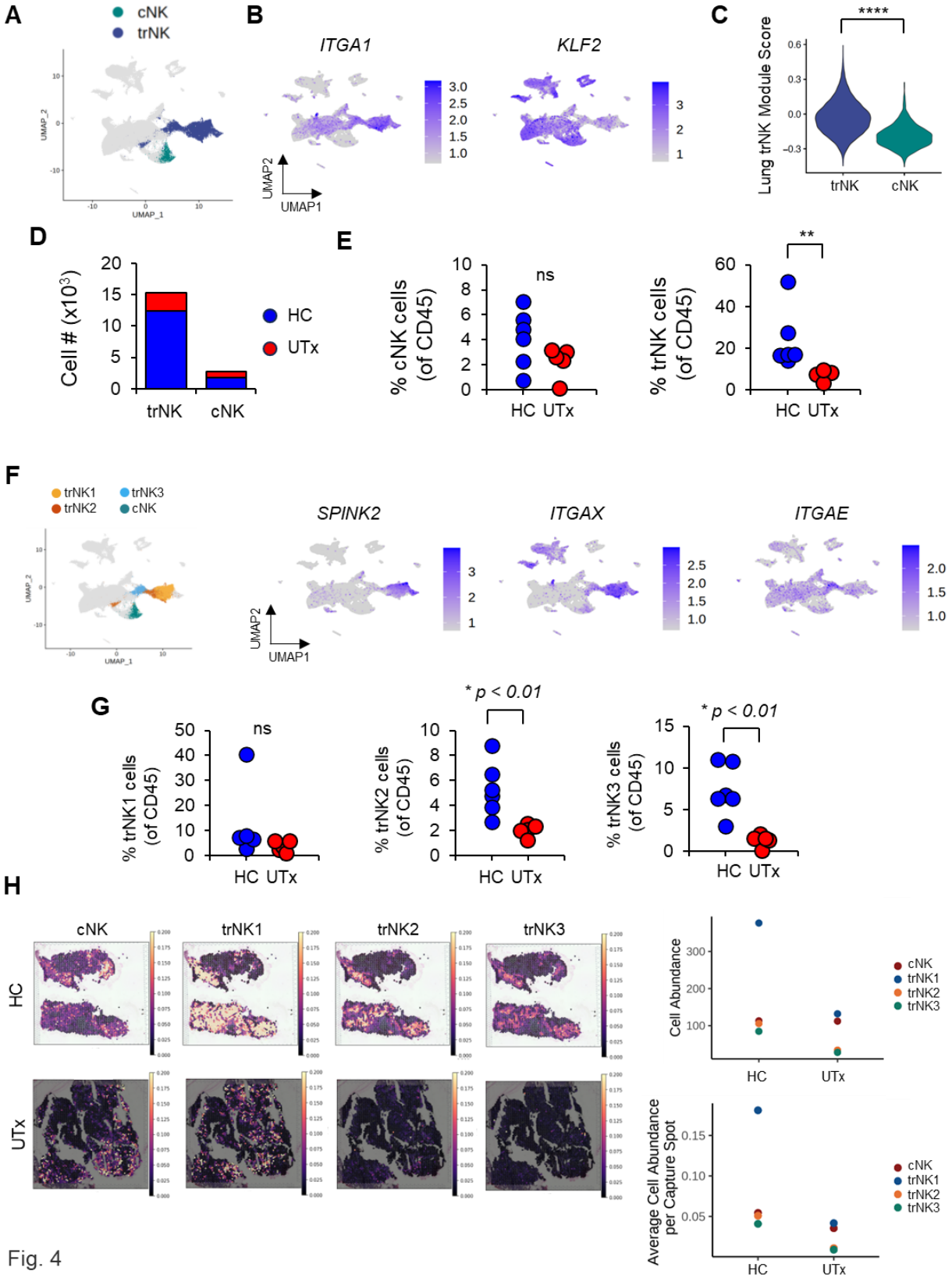
A
cNK
trNK
UMAP_2
UMAP_1
B
ITGA1
KLF2
UMAP2
UMAP1
C
****
Lung trNK Module Score
trNK
cNK
D
Cell # (x10^3)
HC
UTx
trNK
cNK
E
ns
% cNK cells (of CD45)
HC UTx
**
% trNK cells (of CD45)
HC UTx
F
trNK1
trNK2
trNK3
cNK
SPINK2
ITGAX
ITGAE
UMAP2
UMAP1
G
ns
% trNK1 cells (of CD45)
HC UTx
* p < 0.01
% trNK2 cells (of CD45)
HC UTx
* p < 0.01
% trNK3 cells (of CD45)
HC UTx
H
cNK
trNK1
trNK2
trNK3
HC
UTx
Cell Abundance
HC
UTx
cNK
trNK1
trNK2
trNK3
Average Cell Abundance per Capture Spot
HC
UTx
cNK
trNK1
trNK2
trNK3

Fig. 4

Figure 4. Reduction of trNK cell frequency in UTx. (**A**) Feature plot of trNK and cNK cells in UMAP of aggregated CD45+ immune cells sorted from secretory phase endometrial biopsies from HC (n=6) and UTx (n=5). (**B**) Reciprocal expression of *ITGA1* and *KLF2* in trNK and cNK. (**C**) Expression of human lung tissue resident NK module score in endometrial NK subsets. ****P<0.0001; Mann Whitney U test. (**D**) Reduced number of trNK and cNK cells in UTx. (**E**) Frequency of cNK and trNK cells among CD45 immune cells by sample. ns=not significant. **P<0.01. Mann Whitney U test. (**F**) Feature plot of trNK subsets and expression of trNK marker genes: *SPINK2* (trNK1), *ITGAX* (trNK2) and *ITGAE* (trNK3). (**G**) Reduced frequency of trNK2 and trNK3 subsets among CD45 endometrial immune cells. **P<0.01. Mann Whitney U test. (**H**) Endometrial NK subset abundance in intact biopsies from HC and UTx as measured by spatial transcriptomics.

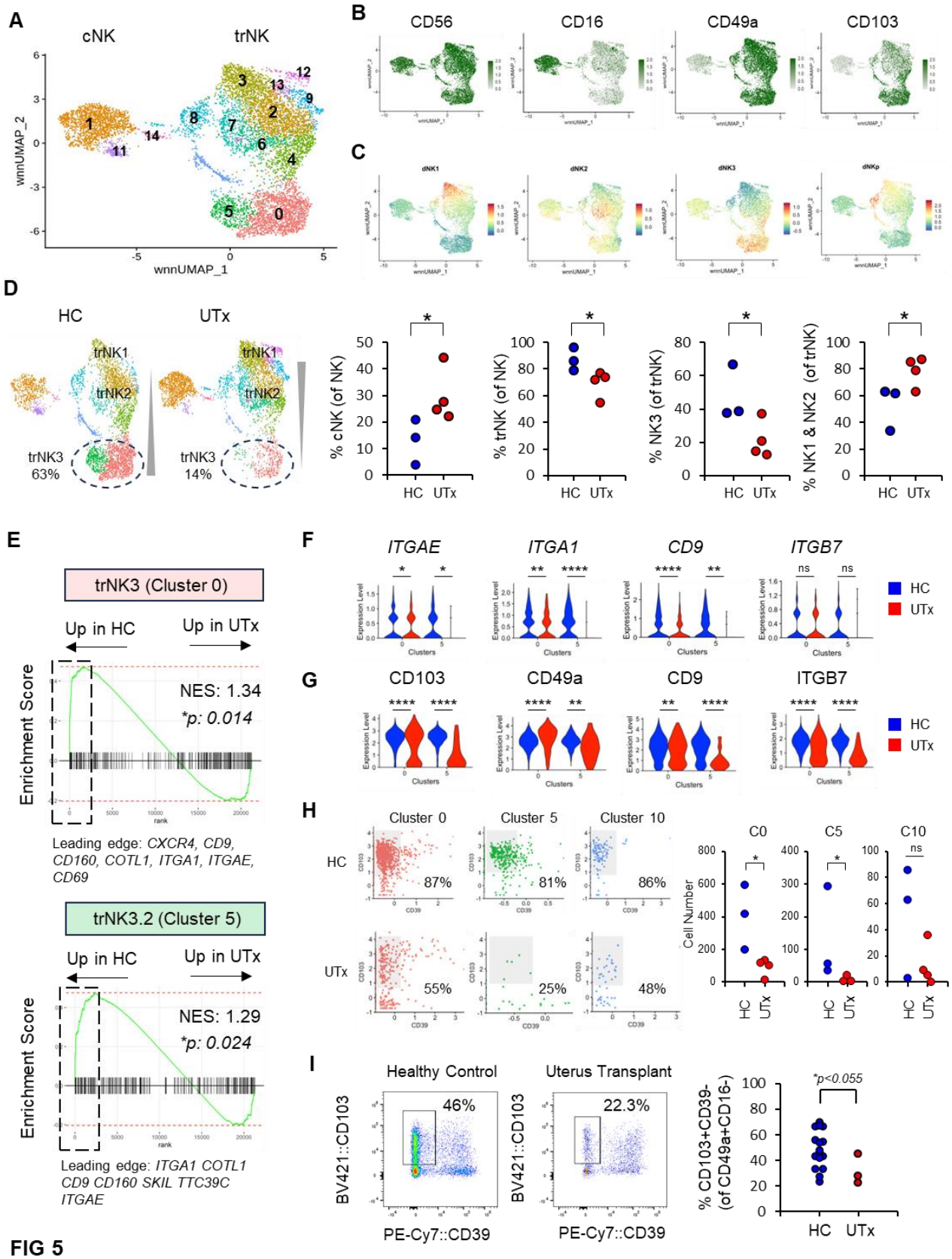
A
cNK
trNK
wnnUMAP_2
wnnUMAP_1
B
CD56
CD16
CD49a
CD103
C
dNK1
dNK2
dNK3
dNKp
D
HC
UTx
trNK1
trNK2
trNK3
63%
14%
% cNK (of NK)
% trNK (of NK)
% NK3 (of trNK)
% NK1 & NK2 (of trNK)
E
trNK3 (Cluster 0)
Up in HC
Up in UTx
Enrichment Score
NES: 1.34
*p: 0.014
Leading edge: CXCR4, CD9, CD160, COTL1, ITGA1, ITGAE, CD69
trNK3.2 (Cluster 5)
NES: 1.29
*p: 0.024
Leading edge: ITGA1 COTL1 CD9 CD160 SKIL TTC39C ITGAE
F
ITGAE
ITGA1
CD9
ITGB7
Expression Level
Clusters
HC
UTx
G
CD103
CD49a
CD9
ITGB7
H
Cluster 0
Cluster 5
Cluster 10
87%
81%
86%
55%
25%
48%
C0
C5
C10
Cell Number
I
Healthy Control
Uterus Transplant
46%
22.3%
BV421::CD103
PE-Cy7::CD39
% CD103+CD39- (of CD49a+CD16-)
*p<0.055

FIG 5

Figure 5. Impairment of TGFβ-mediated tissue residency programs is associated with loss of trNK subsets in UTx. (**A**) Weighted nearest neighbor UMAP of endometrial NK cells in aggregated secretory phase endometrial biopsies from three HC and 4 UTx (n=7 biopsies). Figure portrays analysis of 8,080 NK cells after re-clustering from CD45+ data. (**B** and **C**) Feature plots of indicated proteins and decidual NK signature scores. (**D**) Loss of trNK3 subsets (clusters 0 & 5; dashed line) in UTx with skewing towards cNK and trNK1 subsets (clusters 1 & 3, respectively). Blue=HC; UTx=Red. *P<0.03, one-sided Mann Whitney U test. (**E**) Enrichment of genes upregulated by TGFβ in healthy control trNK3 subsets. (**F** and **G**) Downregulation of key trNK3 subset genes (F) and proteins (G) by UTx compared to HCs. *P<0.05; **P<0.01; ***P<0.001; ****P<0.0001; ns=not significant; Mann Whitney U test. (**H**) Reduction of frequency of CD103+ CD39- in trNK3 clusters in UTx. Numbers in scatter plots indicate frequency of CD103+CD39- cells within indicated cluster. *P<0.03, one-sided Mann Whitney U test. (**I**) Confirmation of reduction of trNK3 frequency in UTx samples by flow cytometry.

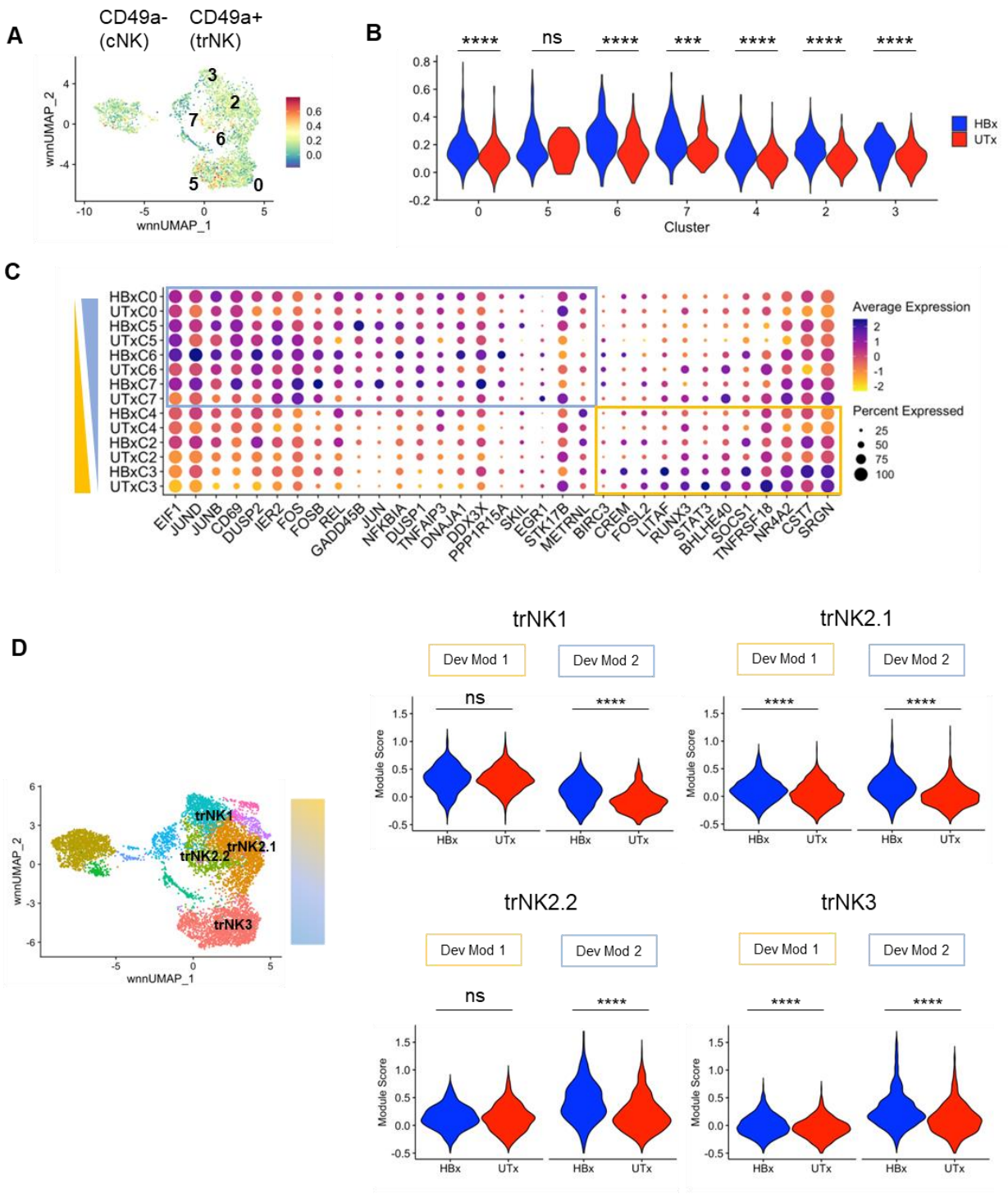
A
CD49a-
(cNK)
CD49a+
(trNK)
wnnUMAP_2
wnnUMAP_1
B
****
ns
***
Cluster
HBx
UTx
C
Average Expression
Percent Expressed
HBxC0
UTxC0
HBxC5
UTxC5
HBxC6
UTxC6
HBxC7
UTxC7
HBxC4
UTxC4
HBxC2
UTxC2
HBxC3
UTxC3
EIF1
JUND
JUNB
CD69
DUSP2
IER2
FOS
FOSB
REL
GADD45B
JUN
NFKBIA
DUSP1
TNFAIP3
DNAJA1
DDX3X
PPP1R15A
SKIL
EGR1
STK17B
METRNL
BIRC3
CREM
FOSL2
LITAF
RUNX3
STAT3
BHLHE40
SOCS1
TNFRSF18
NR4A2
CST7
SRGN
D
trNK1
trNK2.1
trNK2.2
trNK3
Dev Mod 1
Dev Mod 2
Module Score

Fig. 6

Figure 6: Reduced expression of early tissue residency developmental program in UTx trNKs. (**A**) Expression of the early developmental program (EDP) of tissue residence in human endometrial NK cells. (**B**) Reduced expression of the EDP in UTx trNKs compared to HCs. (**C**) Reciprocal expression of two developmental modules in trNK1 and trNK3. (**D**) Left: Consolidation of trNK clusters into four groups based on expression of the EDP. Colored bar reflects direction of developmental module expression across the clusters on the UMAP. Right: More pronounced reduction of developmental module 2 (inclusive of AP-1 transcription factors) than developmental module 1 in UTx trNK subsets. ***P<0.001. ****P<0.00001. Mann Whitney U test.

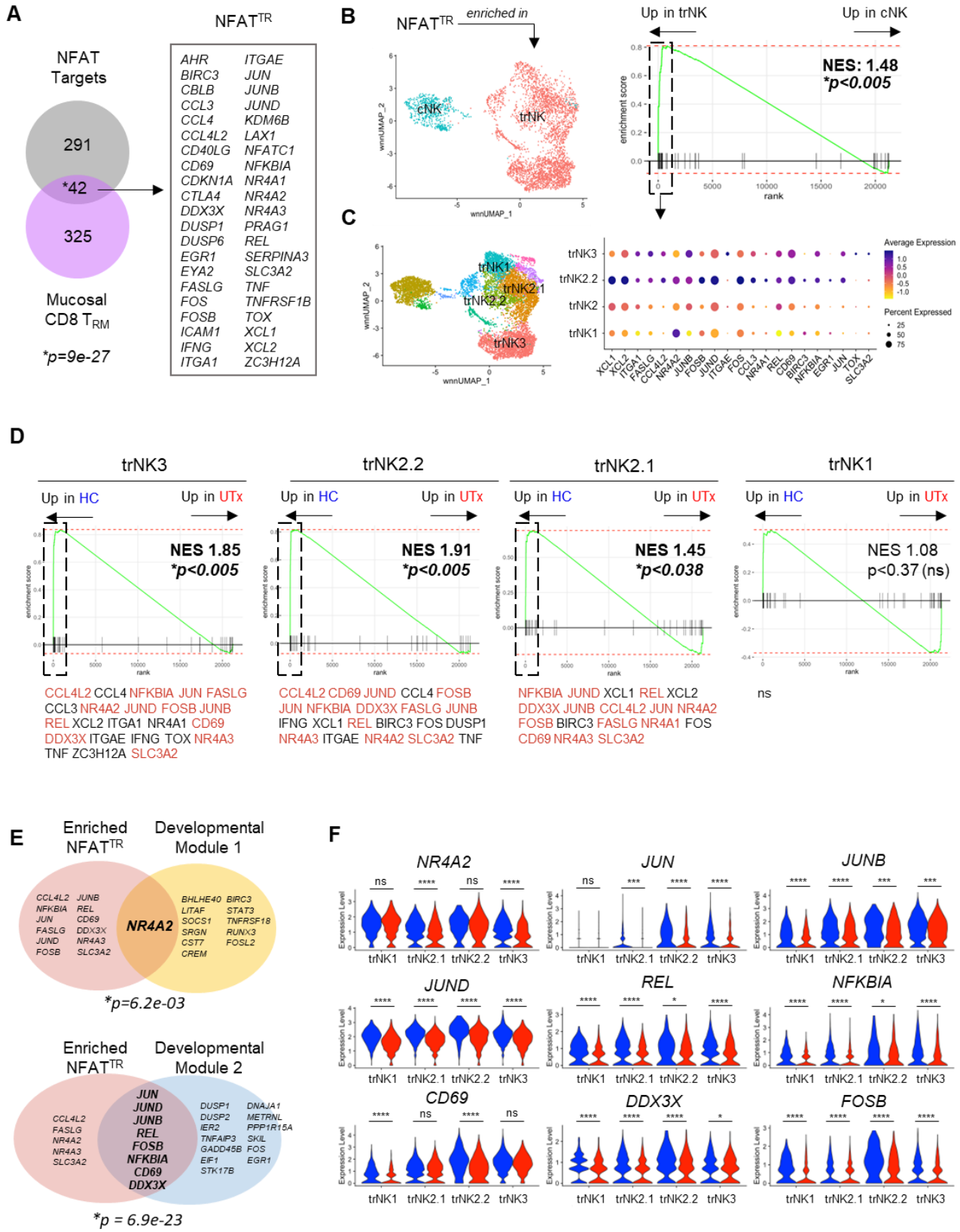
A
NFAT Targets
291
*42
325
Mucosal CD8 T_RM
*p=9e-27
NFAT^TR
AHR ITGAE
BIRC3 JUN
CBLB JUNB
CCL3 JUND
CCL4 KDM6B
CCL4L2 LAX1
CD40LG NFATC1
CD69 NFKBIA
CDKN1A NR4A1
CTLA4 NR4A2
DDX3X NR4A3
DUSP1 PRAG1
DUSP6 REL
EGR1 SERPINA3
EYA2 SLC3A2
FASLG TNF
FOS TNFRSF1B
FOSB TOX
ICAM1 XCL1
IFNG XCL2
ITGA1 ZC3H12A
B
NFAT^TR enriched in
cNK
trNK
wnnUMAP_1
wnnUMAP_2
Up in trNK
Up in cNK
NES: 1.48
*p<0.005
enrichment score
rank
C
trNK1
trNK2.1
trNK2.2
trNK3
Average Expression
Percent Expressed
XCL1 XCL2 ITGA1 FASLG CCL4L2 NR4A2 JUNB FOSB JUND ITGAE FOS CCL3 NR4A1 REL CD69 BIRC3 NFKBIA EGR1 JUN TOX SLC3A2
D
trNK3
Up in HC
Up in UTx
NES 1.85
*p<0.005
CCL4L2 CCL4 NFKBIA JUN FASLG CCL3 NR4A2 JUND FOSB JUNB REL XCL2 ITGA1 NR4A1 CD69 DDX3X ITGAE IFNG TOX NR4A3 TNF ZC3H12A SLC3A2
trNK2.2
NES 1.91
*p<0.005
CCL4L2 CD69 JUND CCL4 FOSB JUN NFKBIA DDX3X FASLG JUNB IFNG XCL1 REL BIRC3 FOS DUSP1 NR4A3 ITGAE NR4A2 SLC3A2 TNF
trNK2.1
NES 1.45
*p<0.038
NFKBIA JUND XCL1 REL XCL2 DDX3X JUNB CCL4L2 JUN NR4A2 FOSB BIRC3 FASLG NR4A1 FOS CD69 NR4A3 SLC3A2
trNK1
NES 1.08
p<0.37 (ns)
ns
E
Enriched NFAT^TR
Developmental Module 1
CCL4L2 JUNB NFKBIA REL JUN CD69 FASLG DDX3X JUND NR4A3 FOSB SLC3A2
NR4A2
BHLHE40 BIRC3 LITAF STAT3 SOCS1 TNFRSF18 SRGN RUNX3 CST7 FOSL2 CREM
*p=6.2e-03
Enriched NFAT^TR
Developmental Module 2
CCL4L2 FASLG NR4A2 NR4A3 SLC3A2
JUN JUND JUNB REL FOSB NFKBIA CD69 DDX3X
DUSP1 DNAJA1 DUSP2 METRNL IER2 PPP1R15A TNFAIP3 SKIL GADD45B FOS EIF1 EGR1 STK17B
*p = 6.9e-23
F
NR4A2
JUN
JUNB
JUND
REL
NFKBIA
CD69
DDX3X
FOSB
Expression Level
trNK1 trNK2.1 trNK2.2 trNK3

Fig. 7

Figure 7: Reduction of NFAT-dependent tissue residency programs in UTx. (**A**) Identification of 42 NFAT-dependent genes involved in tissue residency programming ($NFAT^{TR}$ signature). (**B**) Enrichment of the $NFAT^{TR}$ signature in endometrial trNKs versus cNKs. (**C**) Variable expression of leading edge genes of the $NFAT^{TR}$ across trNK subsets. (**D**) Enrichment of the endometrial $NFAT^{TR}$ signature in healthy control trNK2 and trNK3 subsets. (**E**) Significant overlap of the endometrial $NFAT^{TR}$ signature with tissue residency developmental module 2. (**F**) Expression of genes in HC and UTx which overlapped between the $NFAT^{TR}$ signature and the tissue residency developmental modules. *P<0.05; **P<0.01; ***P<0.001; ****P<0.0001; ns=not significant; Mann Whitney U test.

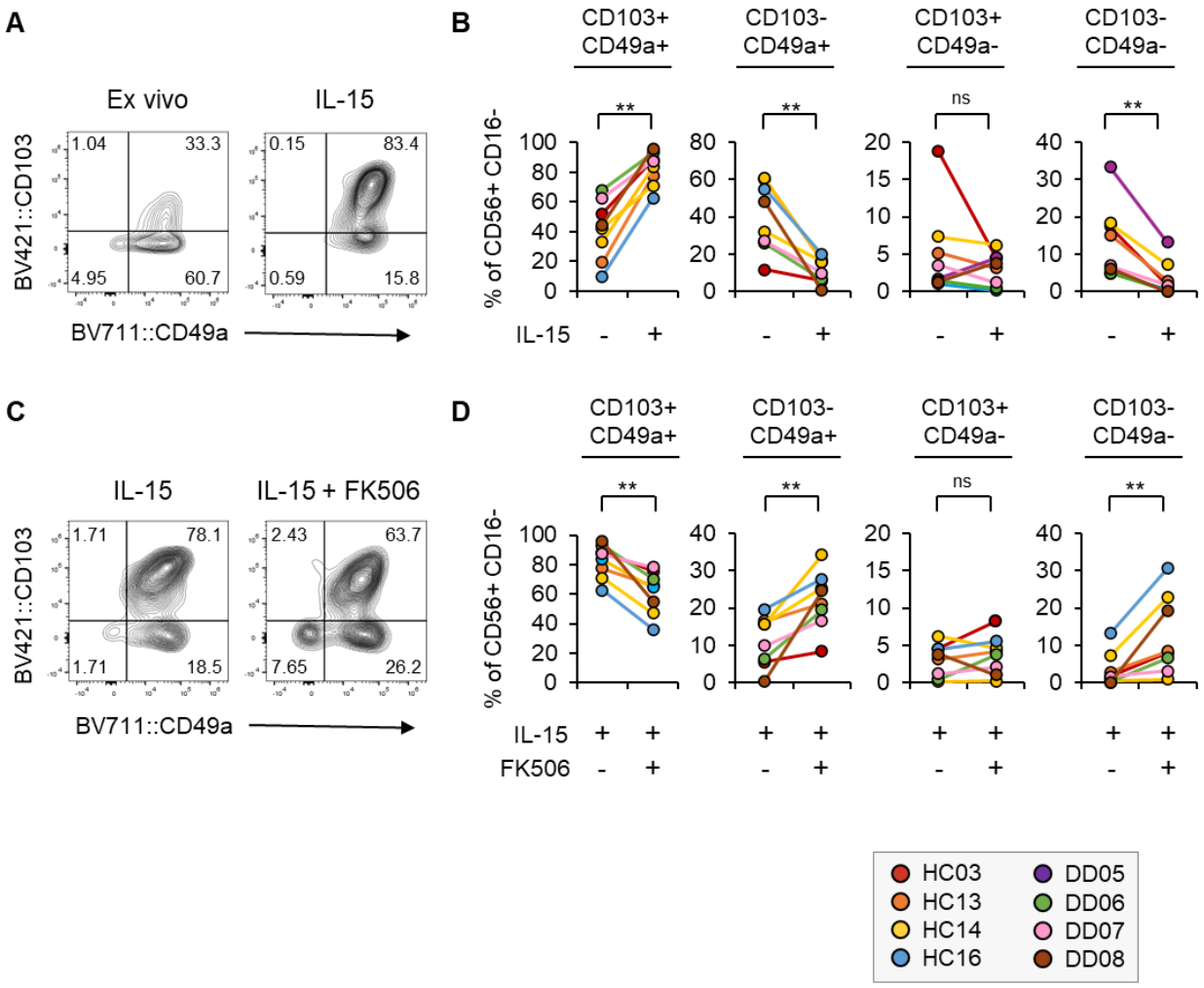
A
Ex vivo
IL-15
BV421::CD103
1.04
33.3
4.95
60.7
0.15
83.4
0.59
15.8
BV711::CD49a
B
CD103+ CD49a+
CD103- CD49a+
CD103+ CD49a-
CD103- CD49a-
% of CD56+ CD16-
**
ns
IL-15
C
IL-15
IL-15 + FK506
1.71
78.1
1.71
18.5
2.43
63.7
7.65
26.2
D
FK506
HC03
HC13
HC14
HC16
DD05
DD06
DD07
DD08

Fig. 8

Figure 8: NFAT blockade impairs IL-15-induced integrin expression on NK cells. (**A** and **B**) Increase in trNK3 frequency after IL-15 culture in vitro. Secretory phase endometrial biopsies from healthy control volunteers (n=4) (HC) and uteri from deceased donors (DD) (unknown menstrual cycle state) (n=4) were collected and single cell suspension were cultured in vitro under the indicated conditions for 4-7 days. Analysis was performed with flow cytometry. Flow panels indicate representative data. **P<0.01; ns=not significant; paired Wilcoxon signed rank exact test.

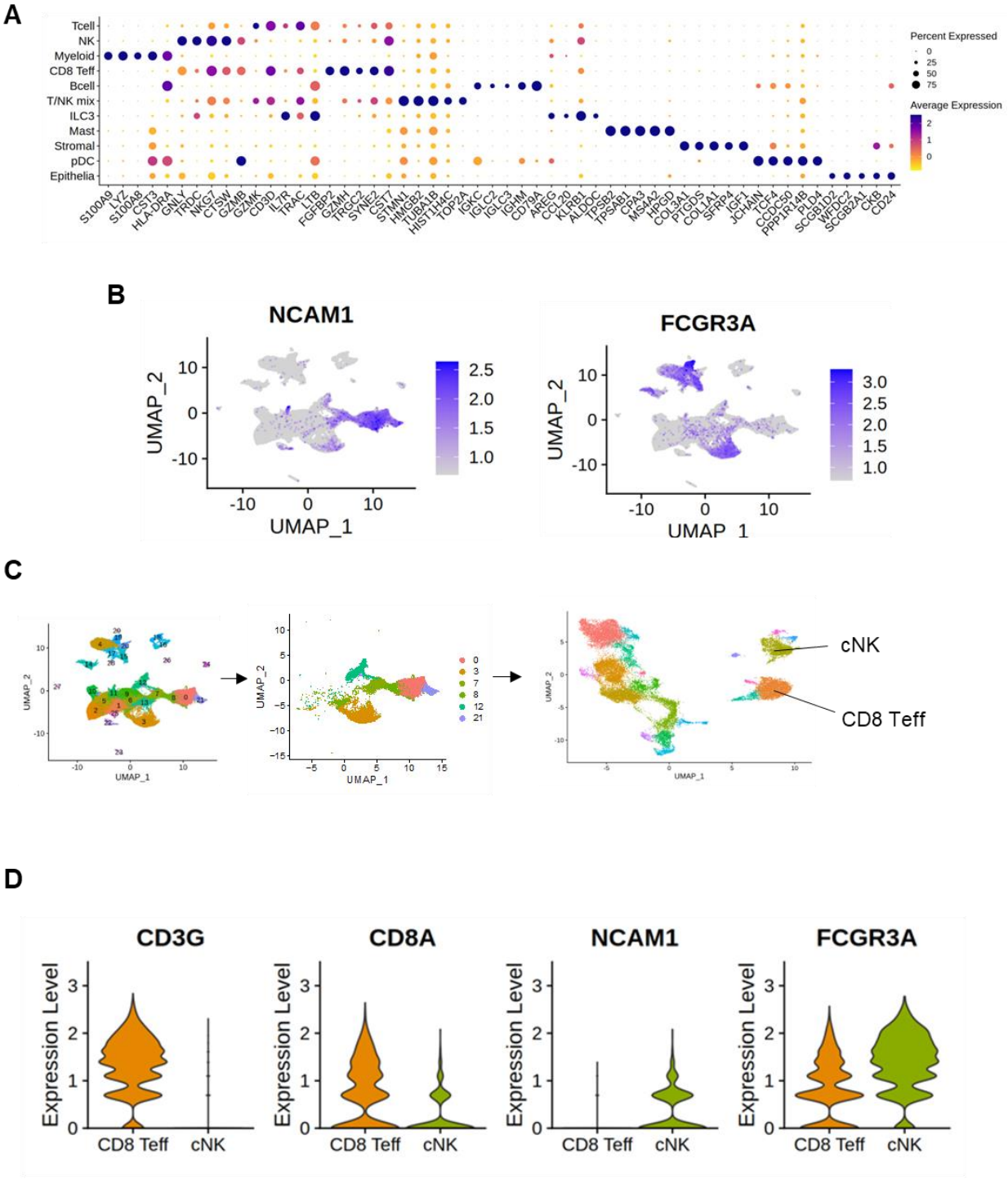
A
Tcell
NK
Myeloid
CD8 Teff
Bcell
T/NK mix
ILC3
Mast
Stromal
pDC
Epithelia
S100A9 LYZ S100A8 CST3 HLA-DRA GNLY TRDC NKG7 CTSW GZMB GZMK CD3D ILTR TRAC LTB FGFBP2 GZMH TRGC2 SYNE2 CST7 STMN1 HMGB2 TUBA1B HIST1H4C TOP2A IGKC IGLC2 IGLC3 IGHM CD79A AREG CCL20 KLRB1 ALDOC TPSB2 TPSAB1 CPA3 MS4A2 HPGD COL3A1 PTGDS COL1A1 SFRP4 IGF1 JCHAIN TCF4 CCDC50 PPP1R14B PLD4 SCGB1D2 WFDC2 SCGB2A1 CKB CD24
Percent Expressed
0
25
50
75
Average Expression
2
1
0
B
NCAM1
UMAP_2
UMAP_1
2.5
2.0
1.5
1.0
FCGR3A
UMAP_2
UMAP_1
3.0
2.5
2.0
1.5
1.0
C
UMAP_2
UMAP_1
0
3
7
8
12
21
cNK
CD8 Teff
D
CD3G
CD8A
NCAM1
FCGR3A
Expression Level
CD8 Teff
cNK

Fig. S1

Supplementary Figure 1. Endometrial immune profiling. (**A**) Marker gene expression for major cell clusters of 77,481 CD45+ cells sorted from 11 secretory phase endometrial biopsies (6HC + 5UTx). (**B**) Expression of major marker genes commonly used to define NK cells: *NCAM1* (CD56) and *FCGR3A* (CD16). (**C**) Distinction of CD8 effector T cells from conventional NK cells. Clusters expressing *NCAM1* and *FCGR3A* (C0,3,7,8,12,21) were selected from CD45+ immune cells and re-clustered. (**D**) Expression of T cell-specific genes (i.e., *CD3G*) as well as *NCAM1* identifies cytotoxic CD8 T cell effectors from cNKs.

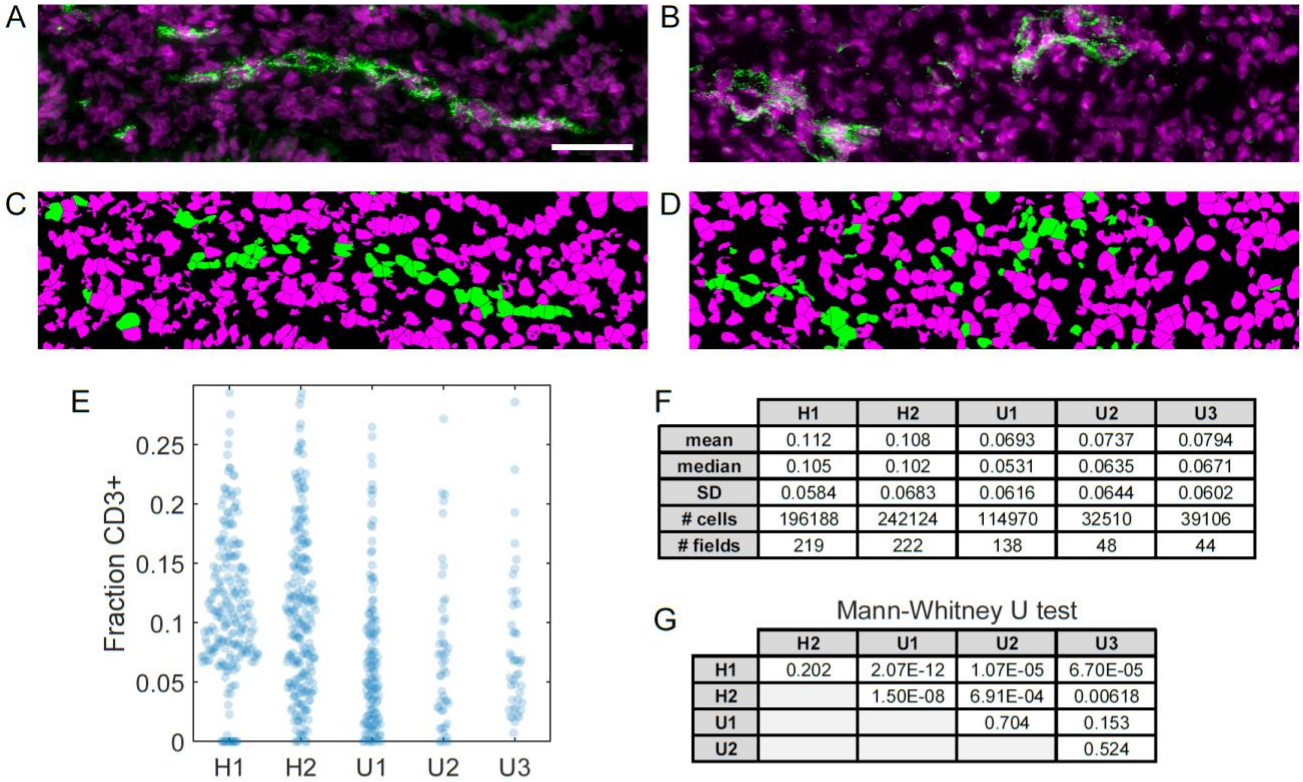

F

	H1	H2	U1	U2	U3
mean	0.112	0.108	0.0693	0.0737	0.0794
median	0.105	0.102	0.0531	0.0635	0.0671
SD	0.0584	0.0683	0.0616	0.0644	0.0602
# cells	196188	242124	114970	32510	39106
# fields	219	222	138	48	44

G

Mann-Whitney U test

	H2	U1	U2	U3
H1	0.202	2.07E-12	1.07E-05	6.70E-05
H2		1.50E-08	6.91E-04	0.00618
U1			0.704	0.153
U2				0.524

Fig. S2

Supplementary Figure 2. CD3-expressing cell density is reduced in transplant endometrium compared to healthy controls. (**A** and **B**) DAPI (magenta) and anti-CD3 (green) staining in health control H1 (A) and transplant U2 (B). Scale bar: 50 µm. (**C** and **D**) Computer rendering of positive (green) and negative (magenta) nuclei in panels A and B. (**E**) Fraction of nuclei designated CD3-positive in healthy control (H1, H2) and uterus transplant (U1-U3) biopsies. (**F**) Summary statistics for the five biopsies. (**G**) p-values (Mann-Whitney U test) for all pairwise comparisons of the five biopsies.

A

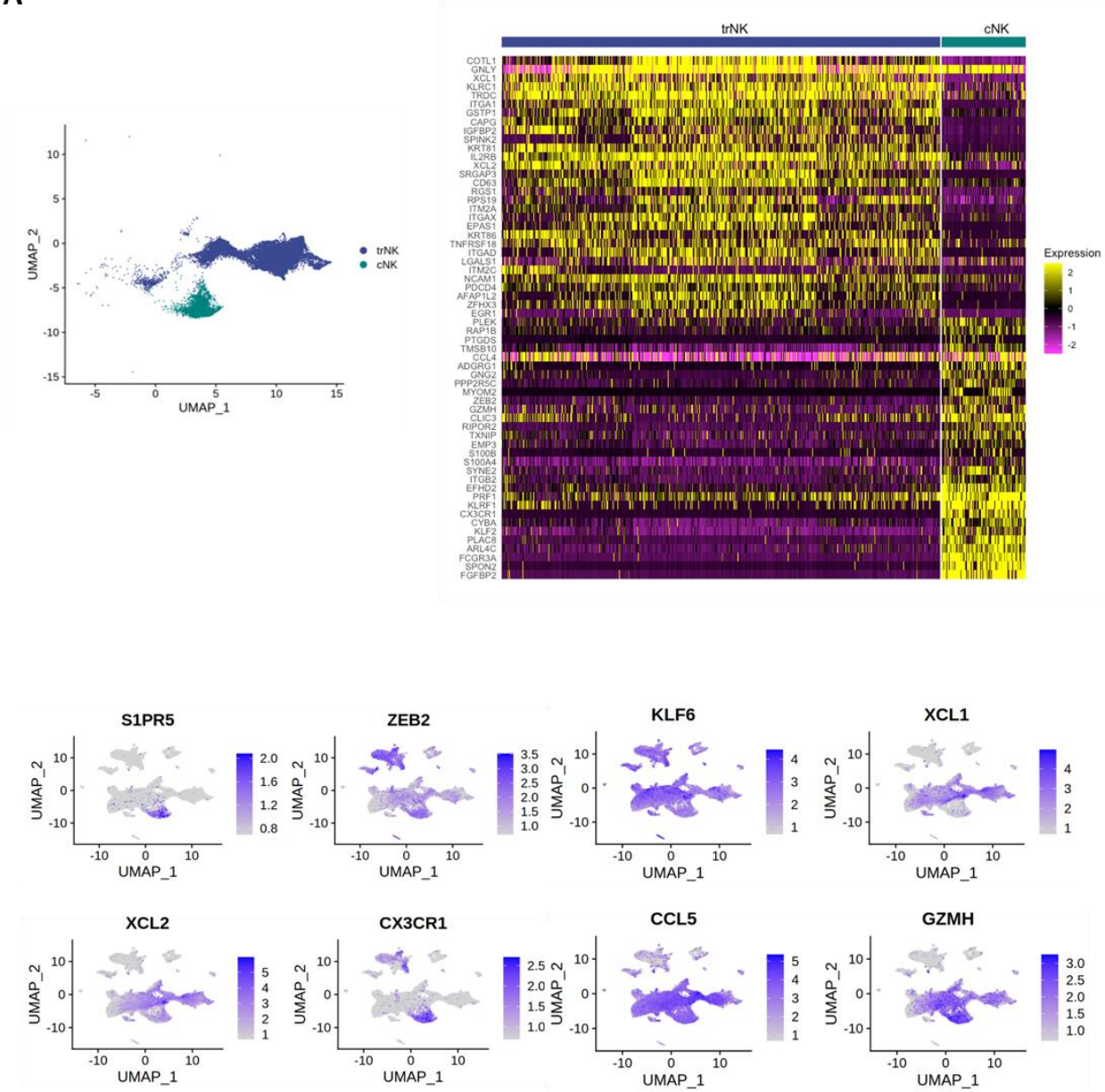
trNK
cNK
UMAP_1
UMAP_2
Expression
S1PR5
ZEB2
KLF6
XCL1
XCL2
CX3CR1
CCL5
GZMH

Fig. S3

Supplementary Figure 3. Identification of trNK and cNK subsets. (**A**) UMAP embedding of endometrial NK subsets with unique transcriptomes for comparison. NK subsets were selected from CD45+ endometrial immune cells enriched from endometrial biopsies (n=11; 6HC+5UTx). (**B**) Heat map of top 30 DEGs between endometrial trNKs and cNKs. (**C**) Feature plots of gene expression in endometrial trNKs and cNKs which associate with either tissue residency or circulatory programs in lymphocytes.

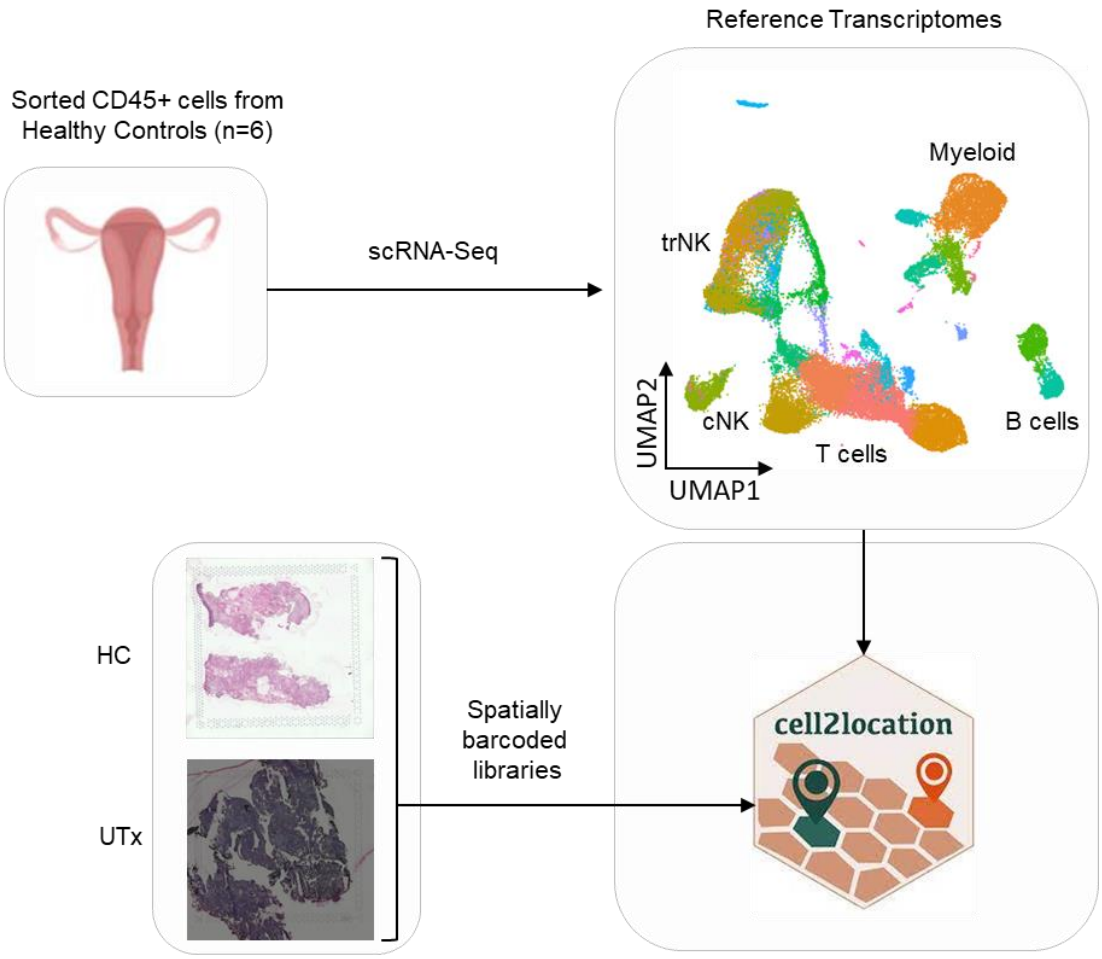
Reference Transcriptomes
Sorted CD45+ cells from
Healthy Controls (n=6)
scRNA-Seq
Myeloid
trNK
cNK
T cells
B cells
UMAP2
UMAP1
HC
UTx
Spatially
barcoded
libraries
cell2location

Fig. S4

Supplementary Figure 4. Cell2location workflow. Spatially barcoded libraries were prepared from one HC secretory phase biopsy and one UTX secretory phase biopsy and input into cell2location along with reference transcriptomes. Reference transcriptomes were derived from aggregated CD45+ endometrial immune cells enriched from HC endometrial biopsies (n=6). Major immune cell clusters are shown for simplicity.

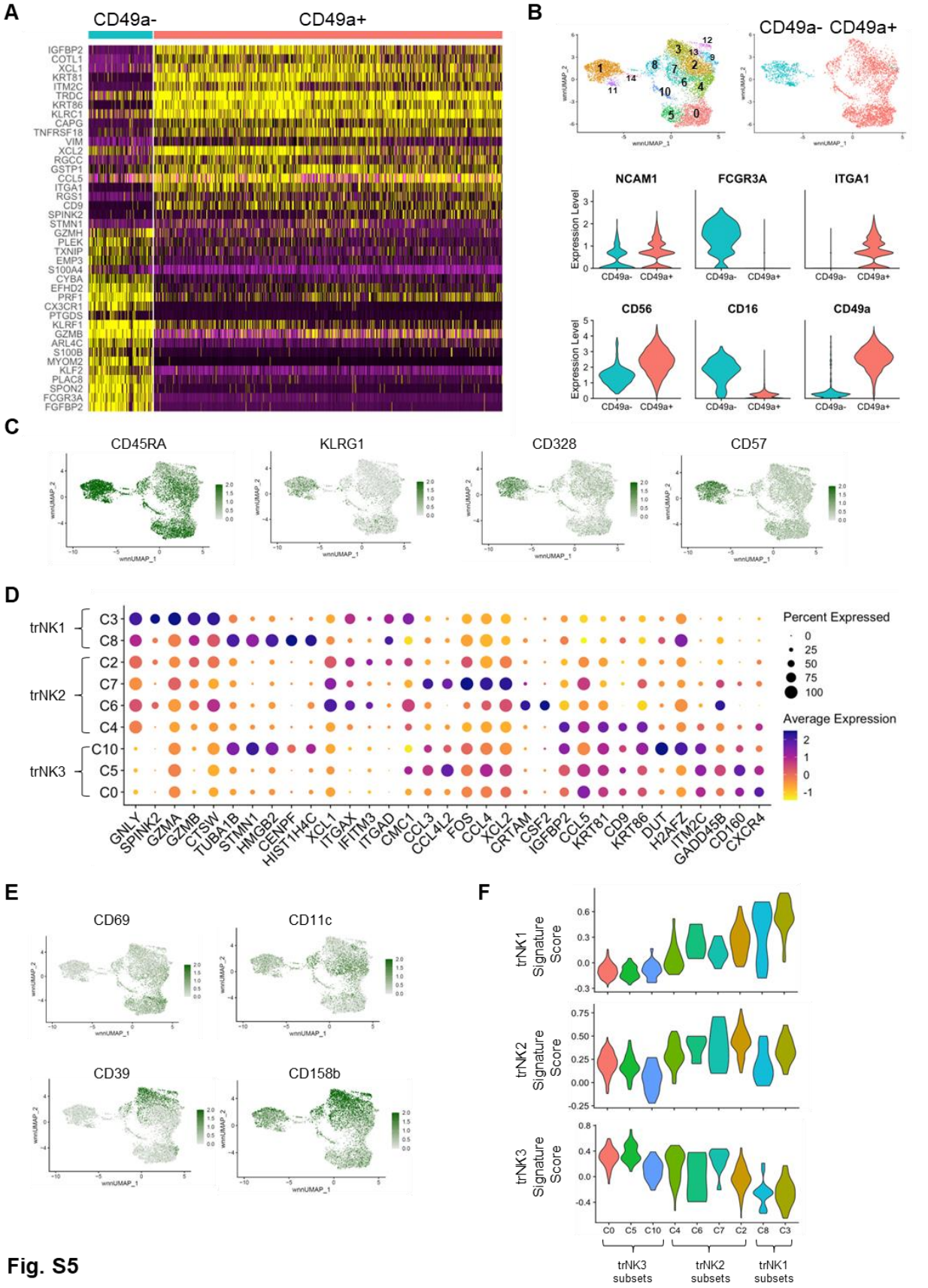
A
CD49a-
CD49a+
IGFBP2
COTL1
XCL1
KRT81
ITM2C
TRDC
KRT86
KLRC1
CAPG
TNFRSF18
VIM
XCL2
RGCC
GSTP1
CCL5
ITGA1
RGS1
CD9
SPINK2
STMN1
GZMH
PLEK
TXNIP
EMP3
S100A4
CYBA
EFHD2
PRF1
CX3CR1
PTGDS
KLRF1
GZMB
ARL4C
S100B
MYOM2
KLF2
PLAC8
SPON2
FCGR3A
FGFBP2
B
CD49a- CD49a+
NCAM1
FCGR3A
ITGA1
CD56
CD16
CD49a
Expression Level
C
CD45RA
KLRG1
CD328
CD57
D
trNK1
trNK2
trNK3
C3
C8
C2
C7
C6
C4
C10
C5
C0
Percent Expressed
Average Expression
GNLY
SPINK2
GZMA
GZMB
CTSW
TUBA1B
STMN1
HMGB2
CENPF
HIST1H4C
XCL1
ITGAX
IFITM3
ITGAD
CMC1
CCL3
CCL4L2
FOS
CCL4
XCL2
CRTAM
CSF2
IGFBP2
CCL5
KRT81
CD9
KRT86
DUT
H2AFZ
ITM2C
GADD45B
CD160
CXCR4
E
CD69
CD11c
CD39
CD158b
F
trNK1 Signature Score
trNK2 Signature Score
trNK3 Signature Score
C0
C5
C10
C4
C6
C7
C2
C8
C3
trNK3 subsets
trNK2 subsets
trNK1 subsets

Fig. S5

Supplementary Figure 5. trNK heterogeneity defined by surface proteome and transcriptomes. (**A**) Top 20 DEGs between CD49a- cNK cells and CD49a+ trNK cells. (**B**) Expression of defining marker genes and surface proteins that identify cNK vs. trNKs in human endometrium. (**C**) Differentially expressed proteins on endometrial cNKs. (**D**) Marker genes identify multiple trNK subsets. Only major subsets are shown. (**E**) Differentially expressed proteins identify major trNK subsets: CD69 (trNK3), CD11c (trNK2) and CD39 and KIRs (trNK1). (**F**) Reciprocal expression of trNK1 and trNK3 gene signatures.

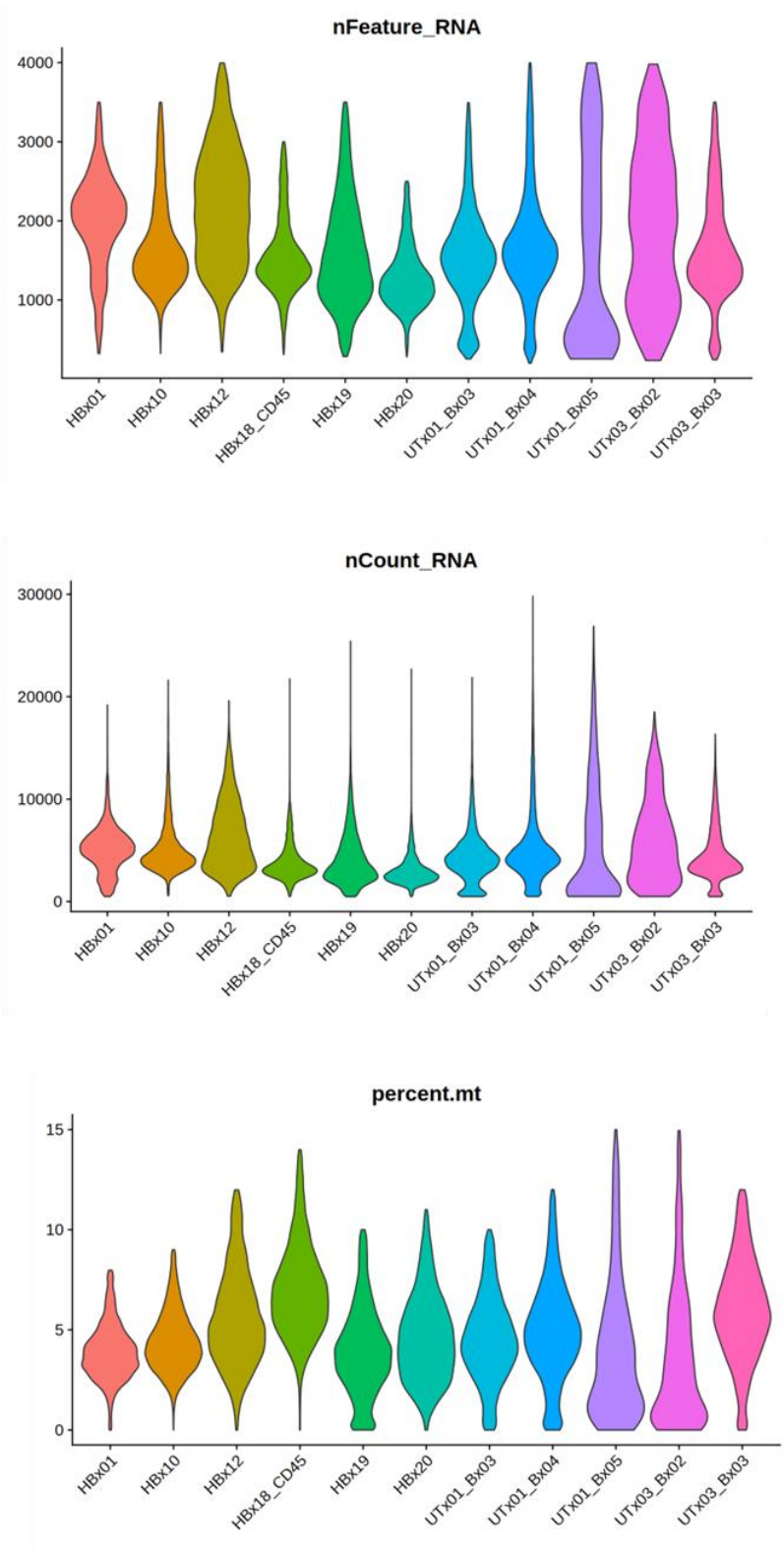
nFeature_RNA
4000
3000
2000
1000
HBx01
HBx10
HBx12
HBx18_CD45
HBx19
HBx20
UTx01_Bx03
UTx01_Bx04
UTx01_Bx05
UTx03_Bx02
UTx03_Bx03
nCount_RNA
30000
20000
10000
0
HBx01
HBx10
HBx12
HBx18_CD45
HBx19
HBx20
UTx01_Bx03
UTx01_Bx04
UTx01_Bx05
UTx03_Bx02
UTx03_Bx03
percent.mt
15
10
5
0
HBx01
HBx10
HBx12
HBx18_CD45
HBx19
HBx20
UTx01_Bx03
UTx01_Bx04
UTx01_Bx05
UTx03_Bx02
UTx03_Bx03

Fig. S6

Supplementary Figure 6. scRNA-seq QC Metrics. Figure portrays expression of key QC metrics for scRNA-seq libraries after filtering with the thresholds as described in “Methods”.